Excessive productivity and heat content in tropical Pacific analyses: Disentangling the effects of in situ and altimetry assimilation

Florent Gasparin [a,*], Sophie Cravatte [b], Eric Greiner [c], Coralie Perruche [a], Mathieu Hamon [a], Simon Van Gennip [a], Jean-Michel Lellouche [a]

[a] Mercator Océan International, 10 Rue Hermès, 31520 Ramonville-Saint-Agne, France
[b] Institut de Recherche pour le Développement (IRD), UMR5566-LEGOS, Toulouse, France
[c] Collecte Localization Satellites, Ramonville-St-Agne, France

ARTICLE INFO

ABSTRACT

Monitoring and predicting global ocean biogeochemistry and marine ecosystems is one of the biggest challenges for the coming decade. In operational systems, biogeochemical (BGC) models are forced – or coupled – with physical ocean models fields that are generally constrained by data assimilation of temperature, salinity and sea level anomalies. Yet, while physical data assimilation substantially improves simulated physical fields, BGC models forced by such analyses are commonly degraded, and more especially in equatorial regions. Here impacts of physical data assimilation on surface chlorophyll and nitrate concentrations are investigated in the tropical Pacific, based on three ocean reanalysis runs using the same physical–BGC model configuration but differing in their level of physical data assimilation. It is shown that, in the Mercator Ocean operational system, the assimilation of satellite altimetry and sea surface temperature in addition to temperature and salinity in situ profiles leads to spurious vertical velocities in the western equatorial Pacific. Our analysis suggests that these unrealistic vertical velocities are explained by the use of an inaccurate mean dynamic topography for the assimilation of altimetry that modifies the pressure-driven horizontal circulation in the upper ocean layer. Moreover, the biases found in this key region modify the subtle dynamical and BGC balances in the whole tropical Pacific and result in unrealistic trends of ocean heat content and nitrate concentration. This study demonstrates that looking into details of the physics is indispensable to improve physical data assimilation systems and to ensure that they make the best use of observations. This is also a key point to refine the strategy of the BGC models forcing and further improve ocean predictions.

1. Introduction

In the tropical Pacific, ocean–atmosphere interactions occurring at different spatial and temporal scales drive the strongest mode of interannual variability, namely, the El Niño-Southern Oscillation (ENSO, Wang et al., 2017). Numerous studies have shown that biogeochemistry and marine ecosystems are significantly affected by the ENSO-related oceanic conditions not only in the tropical Pacific (e.g., Loukos et al., 2000; Radenac et al., 2012), but also in remote regions (e.g., Feely et al., 1995; Martínez-López and Zavala-Hidalgo, 2009; Machado et al., 2013). In turn, phytoplankton concentration in the surface layer can also have significant effects on its physical environment by reducing the solar penetration into the ocean, and thereby affect the temperature and air–sea interaction, and induce positive feedback onto ENSO by heating effects (Park et al., 2018a; Zhang et al., 2019). Significant progress in the understanding of ENSO-related mechanisms has resulted from intense efforts of observation and modeling over the last four

decades (Guilyardi et al., 2016; Chen et al., 2018). Yet important biases in physical and biogeochemical (BGC) models remain and limit our understanding of ocean mechanisms occurring at local-to-global scales and over diurnal-to-multidecadal periods.

In this context, physical ocean reanalyses are a powerful tool that combines information from model dynamics, surface fluxes and observation data sets to provide a dynamically consistent ocean state in the four dimensions (Storto et al., 2019). Following the development of remote sensing and in situ observations, together with progress in modeling and data assimilation techniques, these relevant monitoring tools are now identified as a centerpiece of climate research (e.g., Mayer et al., 2018). Unlike non-assimilative ocean models, reanalyses benefit from multivariate ocean data assimilation and model bias mitigation methods serving as a constraint to reduce systematic biases and long-term drifts resulting from errors in initialization, air–sea flux

formulation and process parameterization. Compared to objective analyses only based on observations, ocean reanalyses use model dynamics counteracting the lack of information in sparsely observed regions.

To monitor and predict ocean biogeochemistry and marine ecosystems, physical ocean reanalyses are now coupled – or used as forcing fields – to BGC or ecological models (Fennel et al., 2019), but counter intuitively physical data assimilation solutions do not systematically produce better BGC fields than non-assimilative solutions (Ford et al., 2018). In fact, BGC fields are even commonly degraded when forced by physics with data assimilation (Ourmières et al., 2009; While et al., 2010; Raghukumar et al., 2015; Park et al., 2018b). This problem is exacerbated around the equator in global models (While et al., 2010; Park et al., 2018b), but has also been observed in regional models (Raghukumar et al., 2015). In controlling the amount of nutrients and carbon available at the surface ocean, vertical velocity is a key variable for physical–BGC models, and numerous studies have pointed out that spurious vertical velocity is a persistent problem in physical ocean reanalyses. These important implications for BGC models are not restricted to a specific ocean model or data assimilation system (Waters et al., 2017; Ford et al., 2018), and have thus pushed the physical oceanography community to further investigate vertical physics during data assimilation procedures.

Unrealistic vertical velocity results from dynamical imbalance between the wind stress and the pressure gradient of data assimilation updates (Bell et al., 2004). Several studies have proposed specific techniques to prevent the data assimilation from degrading vertical velocity. Burgers et al. (2002) demonstrated that including zonal velocity corrections in geostrophic balance with density corrections improves the representation of equatorial currents. Bell et al. (2004), and more recently Waters et al. (2017), proposed to adapt the pressure (density) correction during the data assimilation step in order to maintain the dynamical balance between the wind stress and the pressure gradient along the equator. A more pragmatic technique consisting in modulating the weight of data assimilation in sensitive regions gives positive results (Park et al., 2018b), but this choice is not fully satisfactory because it reduces the gain of data assimilation on horizontal physics. While encouraging results have been obtained, the vertical velocity issue (associated with issues in other physical variables) remains an important limitation of BGC models (Ford et al., 2018).

Here, we address this specific issue in the Mercator Ocean system focusing on the tropical Pacific Ocean, based on an ensemble of three 7-yr physical ocean reanalysis fields (hydrology and currents) using the same ocean model configuration but varying the complexity and the level of data assimilation. We will show that when the physical solution with both in situ and satellite observations is used as forcing fields for a BGC model, unrealistic chlorophyll concentrations are observed in the equatorial band, associated with higher vertical velocity (Section 4). In fact, the assimilation of sea level anomaly requires a reference height, the mean dynamic topography (MDT, defined as the difference between the mean sea surface and the Earth's geoid). Uncertainty on the MDT can significantly impact on the quality of analyses and forecasts (Birol et al., 2004; Vidard et al., 2009; Yan et al., 2015; Hamon et al., 2019) and significant improvements of ocean monitoring systems have been attributed to a more accurate MDT (Lellouche et al., 2018; Guiavarc'h et al., 2019).

The western tropical Pacific is known as a complex region. The main focus here is to detail how the biases of the MDT (here the term "bias" refers to error in the MDT) modify the three-dimensional oceanic circulation in the equatorial Pacific, and eventually, the BGC fields. This study will also determine how the changes in the mean properties can affect the representation of the long-term variability, that remains a challenge for ocean reanalyses (Storto et al., 2019). Even if significant improvement has been achieved for representing the steric sea level interannual variability in ocean reanalyses, large discrepancies between estimates of interannual trends are still observed (Storto et al., 2017). A recent study of Gasparin et al. (2018) showed that global patterns of changes of ocean heat and freshwater contents at interannual

timescales are significantly improved with data assimilation, but the amplitude is two times stronger than estimates from observations. We will show here that biases in the MDT can produce unrealistic long-term drift of the thermosteric component of the steric sea level through modifications of the ocean heat content.

In the following we begin with a description of the physical–BGC model and the in situ and satellite observation products (Section 2) which have been used to demonstrate the sensitivity of the physics and biogeochemistry to the level of physical data assimilation (Section 3). Then some simple dynamical arguments are given in Section 4 to demonstrate how the use of a biased MDT for the assimilation of altimetry causes unrealistic upwelling by reducing the horizontal convergence in the western equatorial Pacific. Finally, the sensitivity of the evolution of the ocean heat content to the changes of the mean oceanic circulation is analyzed in light of previous results in Section 5. Conclusion and discussion are provided in Section 6.

2. Ocean reanalysis simulations, assimilation experiments and validation data sets

2.1. Physical model and data assimilation procedures

This work is mainly built upon a series of three 7-yr global ocean simulations which have been performed in the context of the global high resolution ocean monitoring and forecasting system operated in near real time by the Copernicus Marine Environment Monitoring Service (CMEMS) since 19 October 2016. These runs have been originally presented in Lellouche et al. (2018). The system was run from October 2006 to October 2016 toward the real-time regime, assimilating the reprocessed observations (along-track altimetric sea level anomaly, SLA; satellite sea surface temperature, SST; sea ice concentration; in situ temperature and salinity vertical profiles, T/S profiles). To quantify impacts of the main different components of the assimilation system, two other twin numerical simulations, that use the same ocean model configuration but that differ by their assimilation level of observation data sets, have been performed over a similar period, October 2006–December 2014.

The model component is based on the version 3.1 of the NEMO ocean model, with a 1/12° ORCA grid type (with a horizontal resolution of 9 km at the equator, 7 km at mid-latitudes and 2 km near the poles). The water column is composed of 50 vertical levels, including 22 levels within the upper 100 m, with 1-m resolution at the surface and 450-m resolution at the bottom. The forcing atmospheric fields are obtained from the European Centre for Medium-Range Weather Forecasts-Integrated Forecast System (ECMWF-IFS) at 3-h resolution, in order to reproduce the diurnal cycle. This system has been initialized using temperature and salinity profiles from the EN4 monthly gridded climatology (Good et al., 2013), averaged for the period October–December 2006. More details concerning parameterization of the terms included in the momentum, heat and freshwater balances (i.e, advection, diffusion, mixing or surface flux) can be found in Lellouche et al. (2018).

Satellite altimetry, sea surface temperature (SST) and sea ice concentration observations, operationally produced by CMEMS (http://marine.copernicus.eu/), are assimilated in the system. This consists of along-track sea level anomaly data from the Data Unification and Altimeter Combination System (DUACS) multi-mission altimeter products and gridded OSTIA SST (*Operational sea surface temperature and sea ice analysis*), which combines satellite SST data (*Group for High Resolution Sea Surface Temperature* project, GHRSST) with *in-situ* observations (Donlon et al., 2012). Additionally, satellite sea ice concentration from the EUMETSAT/Ocean and Sea Ice Satellite Application Facility (OSI SAF) is assimilated. Subsurface vertical profiles of temperature and salinity from the CORA 4.1 *in situ* database (Cabanes et al., 2013; Szekely et al., 2016) are also assimilated. This database includes vertical temperature and salinity profiles from Argo floats, moorings,

gliders, expendable bathythermograph (XBT) transects, sea mammals, and conductivity-temperature-depth (CTD) casts from oceanographic cruises. Low-quality profiles were excluded after several quality control tests were performed as described in Lellouche et al. (2018).

Observation data sets are assimilated using data assimilation techniques, detailed in Lellouche et al. (2013, 2018), and only the necessary elements to interpret results are presented here. The main components of the data assimilation procedures are (i) a 3D-Var correction for the slowly evolving large scale error of the model in temperature and salinity, based on in situ T/S profiles over the last month, and (ii) a reduced-order Kalman filter derived from a Singular Evolutive Extended Kalman filter (SEEK, Brasseur and Verron, 2006), with a three-dimensional multivariate modal decomposition of the background error and a 7-day assimilation cycle. This multivariate procedure considers satellite and in situ observations and presumably corrects patterns at smaller spatial and temporal scales (mesoscale activity) than the 3D-Var correction. In practice, temperature and salinity observation are selected depending on the innovation value, defined as the observation minus model forecast equivalent. For the 3D-Var corrections, innovations are considered on a 1-month window (i.e., at a given 7-day cycle and the three previous cycles) and depending on the horizontal distance of the order of 400–500 km in order to map large-scale temperature and salinity corrections. For the assimilation of the SEEK filter, the analysis at a given point is based on surrounded innovations determined by spatial and temporal correlation scales, ranging from 50 to 450 km in the zonal direction, from 50 to 200 km in the meridional direction and from 3 to 15 days. From the innovations and specified observation errors, the SEEK filter generates a localized analysis increment, which is a linear combination of short-scale anomalies from a statistical ensemble representative of the forecast error covariances (Lellouche et al., 2013). The 3D-Var correction and the SEEK increment are applied progressively using the incremental analysis update (IAU) method (another tendency term added in the model prognostic equations), to avoid model shock every week due to the imbalance between the analysis increments and the model physics (Bloom et al., 1996; Benkiran and Greiner, 2008).

To be comparable with the observed SLA provided by altimetry, the model sea surface height (SSH) is converted to SLA relative to a reference mean SSH. Consequently the assimilation procedure of altimetry results in assimilating the altimetric SLA, but also the reference mean SSH. In the context of numerical models having a spherical ellipsoid, the mean SSH is equivalent to the MDT. Several approaches can be adopted. An observation-based MDT, gathering in situ (hydrologic and drifter data) and gravimetric satellites observations, would correct the mean state of the model. However, the use of such MDT can be damaging in some regions due to the inaccuracy of the MDT and/or important model biases (Vidard et al., 2009). Additionally, the spatial resolution of the estimates only based on observations (around 100 km) might not be consistent with that of the model (here at 1/12°). The mean SSH from the model may also be used directly as the MDT. In that case, model biases are not corrected and only temporal and spatial variability embedded in the altimetric anomalies is assimilated. In practice, long-term reanalysis fields are preferred to get a more accurate estimate of the mean sea surface, as done in the ECMWF system in which only T/S observations are assimilated (Zuo et al., 2019). They found large temperature and salinity biases in regions with strong mesoscale eddy activity, i.e., along the western boundary currents and the Antarctic Circumpolar Current. Some systems use a bias correction to correct for biases in the MDT during the assimilation (e.g., Lea et al., 2008).

In the present study, the MDT results from a combination of model and observation-based MDTs following a complex iterative procedure using statistics from the previous reanalysis (GLORYS2V3), the observed MDT CNES_CLS13, the 2014 version of the GRACE and GOCE data as well as the World Ocean Atlas (WOA) 2013 climatology (more details in Hamon et al., 2019). The error variance associated with the MDT estimate is an important information during the assimilation of altimetry to refine the SLA error associated with each satellite (Lellouche

et al. 2018). As error associated with each data set used for the MDT computation is poorly known, a boot-strap estimation method based on the work of Desroziers et al. (2005) is used. In addition, an ensemble method is applied to overcome uncertainty in error statistics such as the correlation function or the error magnitude of each observation data set. The final MDT error (scale of about 150 km) is computed by combining the dispersion of the ensemble members (36 members) with the final error estimates produced by Desroziers et al. (2005). Since the ensemble is relatively small, an amplification of the dispersion is applied to obtain the level estimated by Desroziers et al. (2005). Theoretically, the SLA error is optimal if there is no bias (Desroziers et al., 2005), which is generally the case. However, the equatorial Pacific is a notable exception where there is an inconsistency between sets of observations (not shown), likely related to gravimetric error and/or non-negligible contribution of deep steric height and ocean mass.

2.2. Biogeochemical model

The BGC component of the physical–BGC model is based on the model PISCES (Pelagic Interactions Scheme for Carbon and Ecosystem Studies) distributed in the NEMO framework. Based on coarsening algorithm, the 1/12° physical daily fields have been degraded to the 1/4° horizontal resolution of the BGC model (Aumont et al., 1998) to force the BGC model. Note that the coarsening algorithm allows to conserve the total volume contained in the 1/12° fields and maintain non-divergence (Berthet et al., 2019). PISCES-V2 (Aumont et al., 2015) is a model of intermediate complexity with 24 prognostic variables which simulates the BGC cycles of oxygen, carbon and major nutrients (phosphate, nitrate, iron, silicate) controlling phytoplankton growth. The model has been initialized with the World Ocean Atlas 2013 climatology for nitrate, phosphate, oxygen and silicate (Garcia et al., 2013) and with the GLODAP-V2 (Global Ocean Data Analysis Project-Version 2) climatology for the dissolved inorganic carbon and alkalinity (Lauvset et al., 2016).

2.3. Ocean reanalysis simulations and assimilation experiments

The set of ocean reanalysis fields, including temperature, salinity, three-dimensional velocity and sea surface height variables, is composed of a free simulation with no data assimilation, and two data assimilation simulations; on one hand using only the 3D-Var large-scale correction based on in situ temperature and salinity (T/S) profiles, on the other hand using the 3D-Var correction combined with a multivariate Kalman filter considering T/S profiles and satellite information of sea level anomaly and sea surface temperature. Note that including altimetry is fundamental for constraining the mesoscale structure. To distinguish the three simulations by their level of data assimilation, the first analogous simulation is called "NoAssim" (without any data assimilation) and the second one, which only benefits from the large scale T/S correction using in situ T/S profiles, is called "AssimTS". The simulation serving the operational system, which uses a multivariate SEEK in addition to the large-scale T/S correction, is referred as "AssimALL" (Table 1). As altimetry is assimilated by the mean of the SEEK filter (only used in AssimALL), differences between AssimALL and AssimTS are thus due to the assimilation of altimetry and the use of the SEEK filter. Note that the assimilation of SST is negligible for our study (not shown). The last two simulations, performed over a period of several years with the same model configuration and reprocessed observation data sets, are thus considered as "ocean reanalysis fields". As the ocean model state is stabilized, i.e., it reaches the eddy kinetic energy maximum, in about 6 months in the upper 1000 m with data-assimilation or 12 months without assimilation (Lellouche et al., 2018), the fields have been considered over the 2008–2014 period in this study. It is noteworthy that the issue is not depended on the variability (e.g., vertical velocity differences between simulations are not modulated by El Niño).

Table 1
Main characteristics of the simulations used in this study.

Simulation	Details
Ocean reanalysis simulations, 7-yr period, 1/12° horizontal resolution	
NoAssim	No data assimilation
AssimTS	3D-Var correction, large scale spatial (∼5–6°) and temporal (∼1 month) correction by assimilating only T/S in situ observations
AssimALL	3D-Var correction + SEEK correction (multivariate correction (7 days) by assimilating SST, T/S in situ observations and altimetry)
Assimilation experiments, 1.5-yr period, 1/4° horizontal resolution	
CONTROL	Similar to AssimALL (including the same MDT)
NOALTI	Same as CONTROL, but altimetric data are withheld (T/S profiles are used in the 3D-Var correction and the SEEK filter)
MDTPATCH	Same as CONTROL, but with a modified MDT ("patched MDT")

In addition to the 7-yr simulations, three 1.5-yr extra experiments have been performed to separate the effects on physical and biogeochemical fields due to the MDT for the assimilation of altimetry from those due to the use of the SEEK filter. To reduce computational costs, these experiments are based on an experimental system similar to that of the three reanalysis runs, but at 1/4° horizontal resolution (Hamon et al., 2019) over a 1.5-yr period. The configuration is based on the version 3.1 of the NEMO ocean model with 50 vertical levels forced by the ECMWF-IFS atmospheric fields. The model has been initialized in 1 January 2014, using temperature and salinity profiles from WOA13 (Locarnini et al., 2013; Zweng et al., 2013). Assimilation procedures have used the same datasets as in the AssimALL simulation (i.e., satellite SST, satellite SLA, in situ vertical profiles and sea ice concentration) and the same techniques (the 3D-Var correction and the SEEK filter). The reference experiment, called the CONTROL run, uses the same MDT as AssimALL for the altimetry assimilation, and only differs from AssimALL by the OGCM resolution and the time period. This reference simulation will be compared with a second experiment (NOALTI), in which altimetric data are withheld (T/S profiles are used in the 3D-Var correction and the SEEK filter). To assess the sensitivity of the physical–BGC model to the MDT, a third experiment, named "MDT-PATCH" and only differing from the CONTROL run by the MDT, will uses a "patched MDT". This will be further explained in Section 4.4. These three physical fields have then been used to force the same BGC model than in Section 2.2. The 1-yr segment from June 2014 to May 2015 has been periodically repeated over a 6-yr period to assess the long-term evolution of biogeochemical variables. It is noteworthy that, even if this experimental procedure does not consider any interannual variability and might include discontinuity between repeated segments, the intercomparison of these experiments allows to quantify the effects of physical data assimilation on BGC fields.

2.4. Validation datasets

To evaluate the skills of the different BGC solutions, surface chlorophyll (Chl) estimates from the CMEMS GlobColour product and nitrate fields from WOA18 have been considered. The CMEMS GlobColour product (1997–present) consists in a reprocessed merged Chl product at 4 km spatial resolution based on measurements from several satellite observations; SeaWiFS (1997–2010), MERIS (2002–2012), MODIS Aqua (2002–present), VIIRS-NPP (2012–present) and OLCI-S3 A (2016–present). This product is distributed by CMEMS (Garnesson et al., 2019). The annual mean of nitrates from WOA2018 consists of fields on a 1° × 1° spatial grid, and are obtained from an optimal analysis based on high-quality oceanographic in situ observations over the period 1955–2018 (Garcia et al., 2018).

In addition to BGC variables, gridded monthly in situ temperature and salinity fields have been provided by the SCRIPPS Argo climatology since 2004 for the global ocean (Roemmich and Gilson, 2009; Gasparin et al., 2015), and have been downloaded from the dedicated SCRIPPS Argo website (http://www.argo.ucsd.edu/). This 1° × 1° horizontal resolution product, with 58 pressure levels from the surface to 2000 dbar, is only based on T/S measurements from Argo floats. In addition, monthly averaged vertical profiles of currents estimated from

Acoustic Doppler Current Profilers (ADCP) on TAO/TRITON moorings have been downloaded from the global tropical mooring buoy array (www.pmel.noaa.gov/gtmba/). ADCP are available along the equator at 156°E, 165°E, 170°W, 140°W, 110°W over the whole period. This single instrument datasets are preferred to gridded products including multiple data sources to ensure independence between comparison products.

3. Sensitivity of physics and biogeochemistry to physical data assimilation

As mentioned in the Introduction, the present work has been firstly motivated by a persistent issue in most ocean reanalyses highlighted by over-productive BGC models in the equatorial band likely due to spurious vertical velocity. By comparing with observations, the aim here is to evaluate the model solutions by investigating BGC and physical environments through the surface Chl, the nitrate concentration, and vertical profiles of temperature and horizontal velocity.

3.1. Chlorophyll and nitrates

Fig. 1 shows surface Chl and vertical sections of nitrates (NO_3) along the equator with contours indicating model estimates and color shading is used for the discrepancy from the observation-based product (GlobColour and WOA2018). The surface Chl shows an over-productive eastern Pacific in the three simulations, with an anomaly exceeding 0.10–0.15 mg/m^3 east of 140°W. Whereas this positive anomaly is reduced in AssimTS compared to NoAssim, much stronger Chl concentration anomalies are seen in AssimALL, almost doubling the Chl concentration. In AssimALL, the 0.10 mg/m^3 contour extends farther west toward the western boundary currents that exhibit the strongest anomaly of Chl concentration (>0.20 mg/m^3). Note that the RMS difference between model and satellite observations is more than two times higher in AssimALL (>0.1mg/m^3) than in NoAssim and AssimTS (∼0.05 mg/m^3), and that the correlation is decreased (see Supplementary Figure). In Fig. 1d–f, vertical sections show the comparison of model nitrates with the WOA18 climatology. NoAssim and AssimTS have smaller nitrate vertical gradient compared to WOA18, as seen by the positive anomaly above the thermocline and negative anomaly below. Again the AssimALL solution shows a much stronger concentration that extends all over the basin above the thermocline, and below near the dateline. The strong tightening of the nitrate isocontours over the whole equatorial band suggests that the significant changes of NO_3 concentrations observed in AssimALL are caused by an upward displacement of the water column near the dateline. Note that the mean outgassing of CO_2 to the atmosphere in the tropical Pacific is increased by more than 50% in AssimALL, going from around 0.5 Pg yr^{-1} in NoAssim and AssimTS, consistently with observations (e.g., Ishii et al., 2014), to 0.8 Pg yr^{-1} in AssimALL (not shown).

To identify what explains the nitrate concentration differences between the simulations, the components of the nitrate budget of AssimALL, and differences from AssimTS, are depth-averaged in the equatorial euphotic zone — the base of the euphotic layer is defined as the depth at which the incoming solar radiation represents 1% of
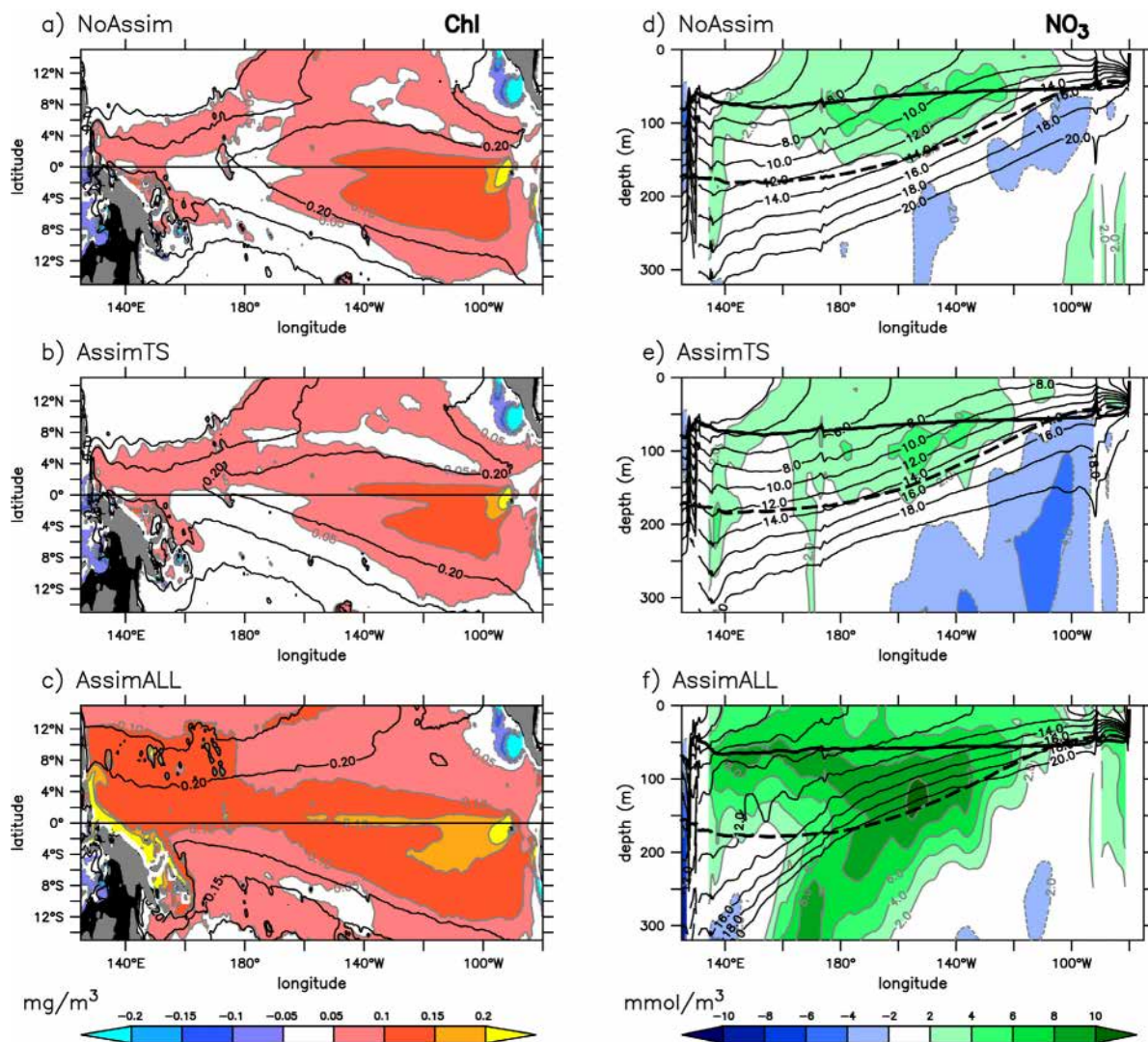
Fig. 1. (a) Map of the 2008–2014 mean of surface Chl concentration (mg/m^3) from the NoAssim estimate (contours) and the discrepancy from GlobColour (color shading). (b) Same as (a), except for AssimTS. (c) Same as (a) except for AssimALL. (d) Equatorial section of the 2008–2014 mean of nitrate concentration (mmol/m^3) from NoAssim estimate (contours) and the discrepancy from the WOA18 climatology. (e) Same as (d) except for AssimTS. (f) Same as (d) except for AssimALL. In (d–f), the thick full and thick dashed lines indicate the base of the euphotic layer, defined as 1% of the photosynthesis available radiation (PAR), and the thermocline depth, defined as the depth of the isopycn $\sigma = 1025$ kg/m^3, respectively.

the photosynthesis available radiation (Fig. 2). Compared to AssimTS, stronger NO$_3$ vertical advection is seen in AssimALL in the western Pacific (including along the boundary), while stronger vertical diffusion is found in the central equatorial Pacific. Both components (vertical advection and diffusion) plus the horizontal advection are the physical drivers bringing nitrates in the euphotic layer (Fig. 2c). It demonstrates that while the focus is traditionally on vertical processes, this is more a three dimensional problem. Biological processes respond to this increased supply as seen in the "sources-minus-sinks" (SMS) term (Fig. 2d). Those are mostly due to the consumption by phytoplankton, consistent with higher Chl in this region as seen in Fig. 1. While the equatorial vertical advection flux has a difference of 0.040 mmol/m^3/day between AssimTS and AssimALL in the western Pacific, the residual of physical and biological processes is of the order 0.001 mmol/m^3/day that accumulates with time (not shown). Consequently, the modification of the NO$_3$ vertical advection in AssimALL brings NO$_3$ rich waters that stimulate the phytoplankton growth. It also changes the nitrate balance between physical drivers and biological response that leads to a higher accumulation of nitrate of the order of O(0.1) mmol/m^3/yr.

Compared to AssimTS, the NO$_3$ vertical advection in AssimALL is mostly characterized by higher values west of the dateline in the euphotic layer and below the thermocline, and above the thermocline east of it (Fig. 3a). These patterns reflect the NO$_3$ stratification (Fig. 1f). To further investigate the causality of NO$_3$ vertical advection differences between AssimALL and AssimTS, it is useful to decompose it to separate changes due to the differences of NO$_3$ concentrations, from those due to the differences of vertical velocity as follows:

$$\overline{w_1 \partial_z N_1} - \overline{w_2 \partial_z N_2} = \underbrace{\frac{\overline{w_1 + w_2}}{2} \partial_z(N_1 - N_2)}_{effects\ of\ NO_3\ diff.} + \underbrace{\overline{(w_1 - w_2)\partial_z \frac{(N_1 + N_2)}{2}}}_{effects\ of\ w\ diff.} \quad (1)$$

with w the vertical velocity, $\partial_z N$ the vertical gradient of NO$_3$ and the indexes 1 and 2 referring to AssimALL and AssimTS respectively.

In Fig. 3b, the effects of the vertical velocity differences are obvious west of the dateline, with a positive anomaly extending from the near-surface to at least 300 m, explaining more than 95% of the vertical advective flux changes. In Fig. 3c, the effects of the differences in NO$_3$ concentration shows a zonal dipole above the thermocline, with negative values west of the date line and positive values east of it. This pattern, explaining more than 95% of the vertical advective flux
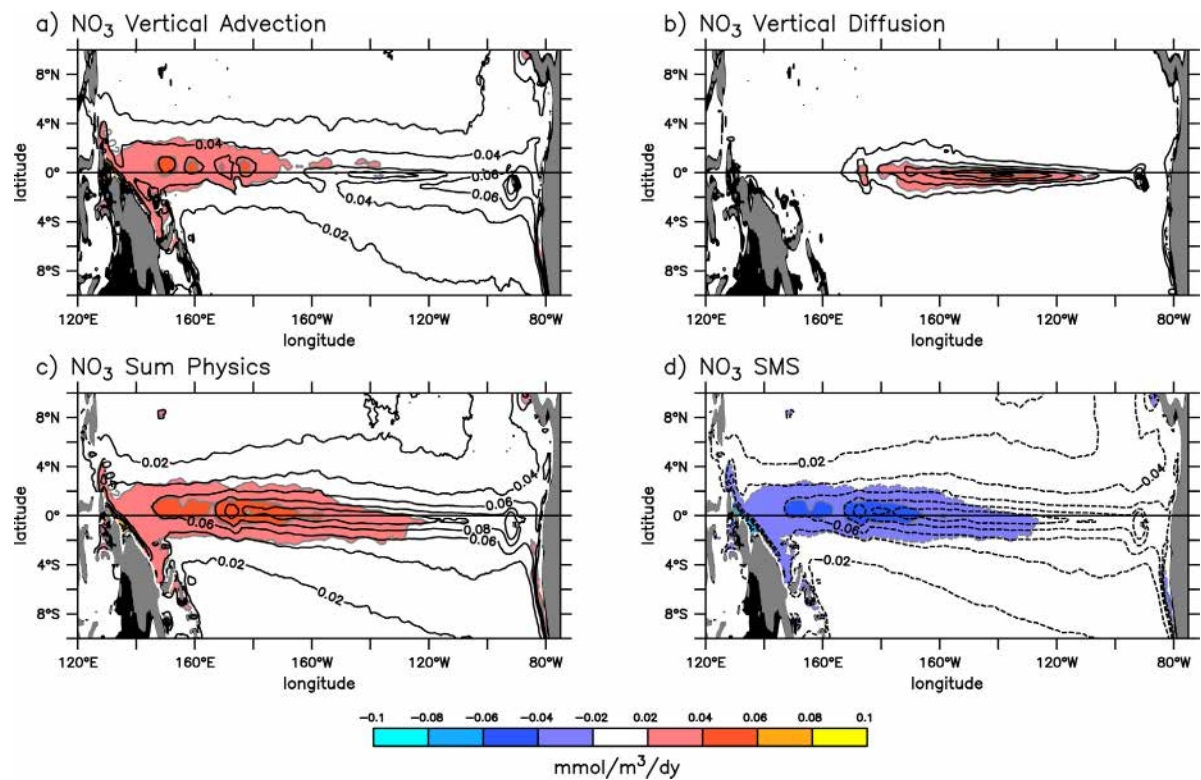
Fig. 2. (a) Map of the 2008–2014 mean of the vertical advection flux of nitrate averaged in the euphotic layer from AssimALL (contours) and the difference from AssimTS (color shading). (b) Same as (a) but for the vertical diffusion flux of nitrate. (c) Same as (a) except for the sum of the fluxes from physics processes (horizontal advection, vertical advection, vertical diffusion). (d) Same as (a) except for the fluxes from biological processes (SMS = source minus sink). Unit is mmol/m^3/day.

changes above 300 m east of the date line, suggests that an important part of the nitrates vertically advected in the western Pacific are then transported to the east by the Equatorial Undercurrent (EUC). This clearly demonstrates the key role of the vertical velocity in the observed changes of the NO_3 concentration that brings rich nitrate waters to the upper layer which are then distributed in the whole equatorial Pacific by the horizontal circulation. Based on a similar decomposition, changes of the diffusion flux ($Kz_1\partial_z N_1 - Kz_2\partial_z N_2$) in the eastern Pacific (Fig. 2b) are mostly due to changes due to the vertical gradient of nitrates, resulting from the supply of waters rich in nitrates by vertical advection (Radenac et al., 2019), rather than changes due to the mixing coefficient K_z (not shown).

Several papers suggest that shocks during the assimilation procedures might cause modification in the mean vertical advection flux (e.g., Raghukumar et al., 2015). In Fig. 3d, boxplots of daily vertical velocity at 100-m are shown at three longitudes in the western equatorial Pacific. The variability of the vertical velocity does not significantly change between both simulations (the whiskers are not longer in AssimALL) as would be expected in the presence of data assimilation shocks. Rather, the largest change is seen in the median vertical velocity with higher values in AssimALL than in AssimTS (~1 m/day). This demonstrates the benefits of the IAU methodology which smooths the impact of assimilation (Benkiran and Greiner, 2008). The mean rate of vertical nutrient input in the western Pacific thus appears to be the key element explaining unrealistic accumulation of Chl in the surface layer in AssimALL.

3.2. Temperature and current profiles

The comparison of the three simulations is now carried out on the physical properties by investigating the changes on the thermal stratification and currents. To provide a basin-scale view, the equatorial thermal structure in the upper 300 m is shown in Fig. 4 at

the locations of four historical TAO/TRITON moorings (147°E, 170°W, 140°W, 110°W) by comparing vertical profiles of the reanalysis fields with the SCRIPPS Argo product. The strongest temperature difference is found at the thermocline level (around 150 m in the west and 100 m in the east), with magnitude reaching more than 2 °C in the eastern Pacific in the NoAssim fields. A cold anomaly above a warm anomaly indicates that the vertical thermal gradient at the thermocline level from the model fields is smaller than that from observations, i.e., the thermocline is too diffuse. The "diffuse thermocline" is a recurring problem in numerical simulations (Stockdale et al., 1998; Tatebe and Hasumi, 2010). Data assimilation in AssimTS and AssimALL successively improves the representation of the thermal structure in the central-eastern Pacific. In the western Pacific, the benefits of data assimilation are only seen in the AssimTS fields in which the vertical thermal gradient at 150 m is slightly improved. By contrast, an important degradation is found in AssimALL with a cold anomaly reaching more than 1 °C at 150 m, therefore suggesting that the thermal stratification in the western equatorial Pacific is strongly sensitive to the physical data assimilation. This confirmed by the Root-Mean-Square (RMS) difference from the TAO 100-m daily temperature computed in the western (147°E, RMS diff. at 0.8 °C, 0.6 °C, 1.0 °C) and central Pacific (140°W, RMS diff. at 1.9 °C, 1.6 °C, 1.2 °C) for NoAssim, AssimTS and AssimALL respectively. Note that using temperature fields from TAO/TRITON moorings having smaller vertical resolution rather than that from the Argo product gives similar results.

The mean zonal velocity fields are then compared with the ADCP current estimates provided by the TAO/TRITON array, by only selecting model time steps corresponding to existing observations for computing the 2008–2014 time-mean. Note that the velocity variables are not assimilated. The amplitude and vertical shape of the subsurface maximum, at the core of the eastward EUC, are well recovered in the NoAssim fields with the west–east tilted shape and a magnitude reaching more than 1 m/s in the core of the EUC. Although still too
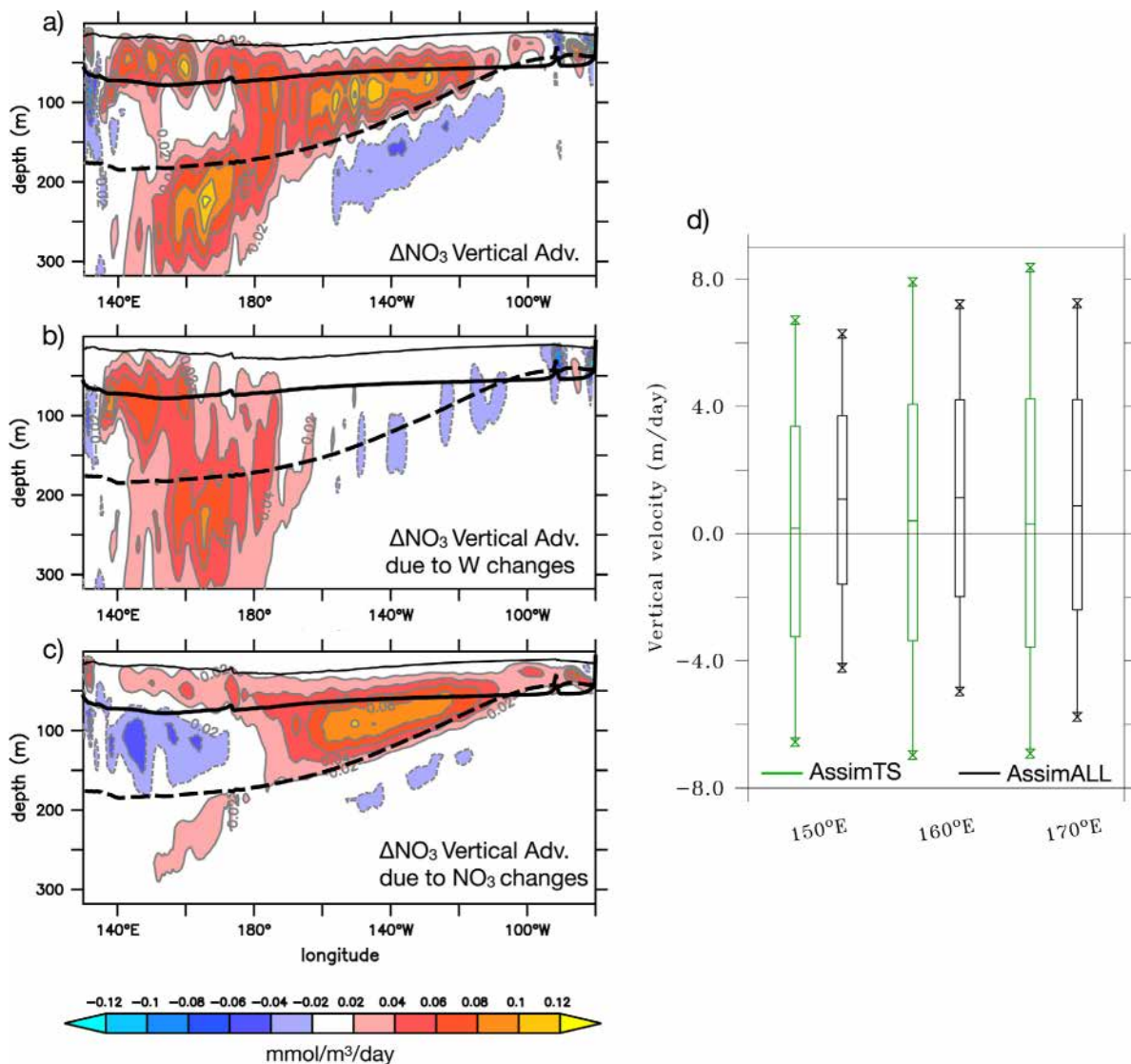
Fig. 3. (a) Equatorial section of AssimALL-minus-AssimTS differences of the vertical advection flux of nitrate time-averaged over the period 2008–2014. The thin full, thick full and thick dashed lines indicate the base of the mixed layer (density criterion of 0.03 kg/m³), the base of the euphotic layer (defined as 1% of the photosynthesis available radiation) and the thermocline depth ($\sigma = 1025$ kg/m³) respectively. (b) Same as (a) except for differences due to the vertical velocity (W) changes. (c) Same as (a) except for differences due to the nitrate concentration changes. (d) Boxplot of the daily vertical velocity at 100 m along the equator averaged in three longitudes in the western Pacific (150°E, 160°E, 170°E) for the period 2008–2014 from AssimTS (green) and AssimALL (black). The whiskers represent the 5th and 95th percentiles.

shallow in the west and too deep in the east, the EUC is much better represented compared to previous studies (Fujii et al., 2015). Similarly to previous conclusions, the two levels of data assimilation reduce the discrepancies between model and observations in the central-eastern Pacific, but not in the western Pacific for the AssimALL solution.

4. What drives the vertical velocity?

To unravel the cause–effect relations between mechanisms resulting from model dynamics and data assimilation procedures, processes at play resulting in an increased vertical velocity in AssimALL are decomposed as individual steps. First, the changes in the upwelling rate are investigated with regards to the horizontal transports. Then, it is demonstrated that most of changes in horizontal circulation are due to the modifications of the pressure field. Finally, we show that biases in the MDT near the western boundary are sufficient to significantly modify the pressure gradient. This point is then supported by dedicated experiments.

4.1. Equatorial upwelling and horizontal circulation

Fig. 5a shows a map of the mean vertical velocity difference between AssimALL and AssimTS at 100 m that exhibits a stronger upwelling between 2°S and 2°N west of the dateline in AssimALL with differences reaching more than 1 m/day in the far western Pacific. The vertical velocity in the ocean model is, by definition, derived online from the continuity equation ($\nabla \cdot \mathbf{u} = 0$, with $\mathbf{u}$ the three dimensional velocity vector), and thus is strictly dependent on horizontal currents. The modification of the horizontal circulation is illustrated by the 0–100 m mass transport, calculated from the velocity fields of the two simulations in two boxes of the western equatorial Pacific between 2°S and 2°N (140°E–165°E and 165°E–170°W; Fig. 5b). The features of the large-scale equatorial circulation are seen on both estimates, that is, the zonal westward flow increasing from east to west is dominated by the South Equatorial Current (SEC), while the easterly trades winds lead to a meridional divergence in the Ekman surface layer (except at the southern side of the westernmost box due to the equatorward western boundary current). The upwelling rate is deduced from the vertical velocity fields, and corresponds to a tight interplay between
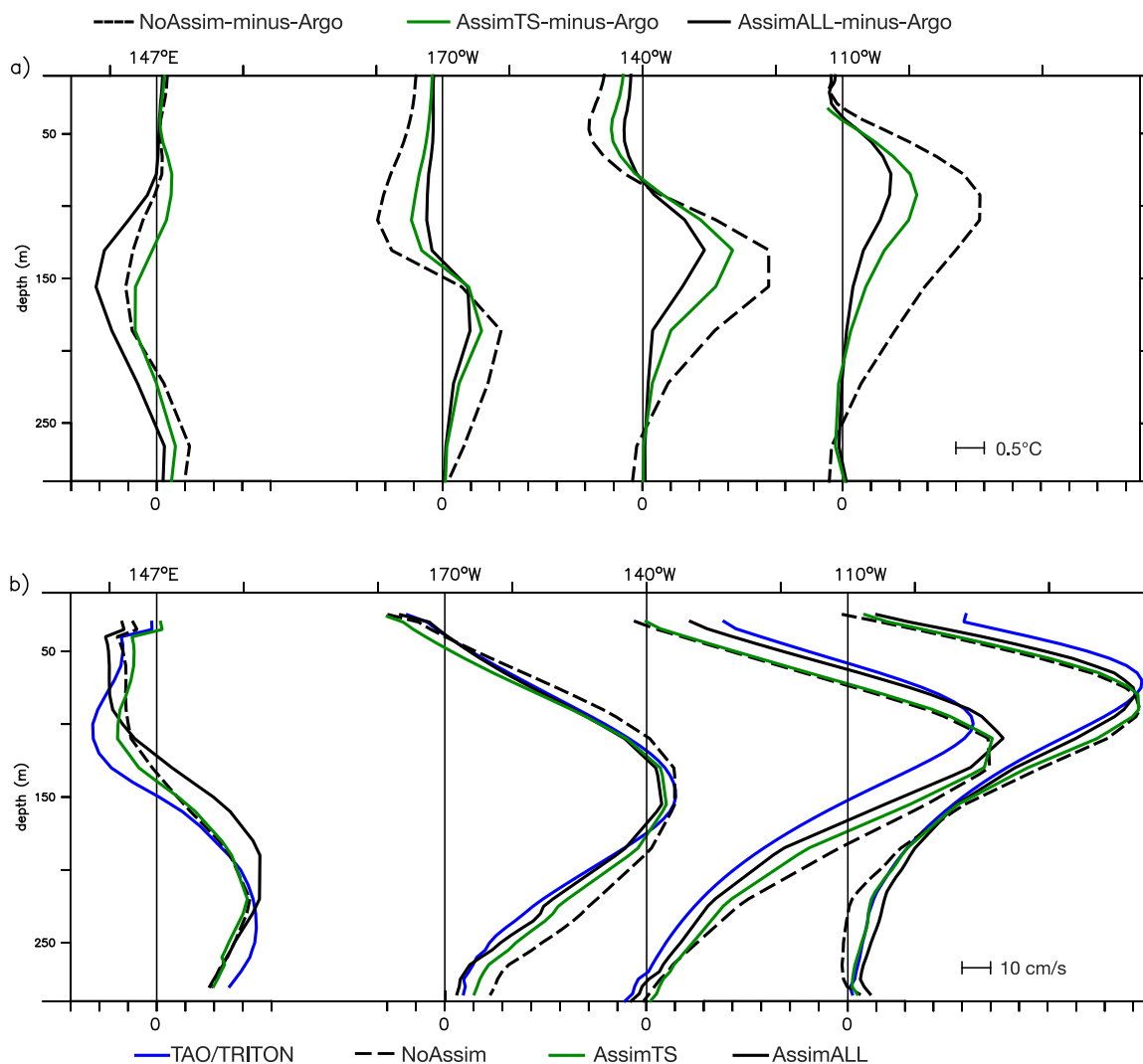
Fig. 4. (a) Profiles of the 2008–2014 mean difference of model temperature from the SCRIPPS Argo product for NoAssim, AssimTS and AssimALL simulations at four equatorial Pacific mooring locations. (b) Profiles of zonal velocity at the same moorings locations from the three simulations and the ADCP (Acoustic Doppler Current Profiler) estimates from the TAO/TRITON mooring array. The graduations in (a) and (b) indicate 0.5 °C and 10 cm/s respectively.

horizontal transports. Though qualitatively similar, the intensity of the upwelling is much higher in AssimALL, especially in the far western Pacific (estimated at 1 Sv in AssimTS and 10 Sv in AssimALL). The increased upwelling in AssimALL (+9 Sv compared to AssimTS) compensates the changes in the meridional (+6 Sv) and zonal (+3 Sv) divergences. In the eastern box, the enhanced zonal divergence in AssimALL (+4 in AssimALL compared to AssimTS) is compensated by a reduced meridional divergence (−1 Sv) resulting in changes of the upwelling rate of 3 Sv in AssimALL compared to AssimTS.

The geostrophic component of the mass transport is shown in Fig. 5c. While the zonal geostrophic component is still westward (the geostrophic approximation can be used for estimating the SEC, Picaut et al., 1989), the geostrophic meridional currents are clearly equatorward. The sum of horizontal geostrophic currents are thus convergent, and most of the upwelling changes can be explained by a reduced meridional convergence in AssimALL due to geostrophy (from 10 Sv to 1 Sv in the western box and from 35 Sv to 30 Sv in the eastern box). The important modifications of the equatorial upwelling are thus the consequences of horizontal changes in both meridional and zonal directions, and can be attributed to the pressure-driven circulation (geostrophic component).

4.2. Sea surface height and steric height

Since most of the modifications of the upwelling rate are related to the pressure-driven circulation, the mean SSH from AssimALL, and the differences from AssimTS, are shown in Fig. 6a. In the northern Pacific, the trough around 8°N and the crest around 4°N mark the edges of the eastward North Equatorial Counter Current, while the large latitudinal extension of the trough south of 4°N indicates the position of the two branches of the westward SEC (Johnson et al., 2002). The meridional tilt of the isocontours reflects the strength of the currents, and shows a maximum in the central and eastern Pacific in agreement with Johnson et al. (2002). The main patterns of the SSH differences are the positive anomaly around 8°N, the two negative lobes in the central Pacific and the strong negative anomaly along the western boundary. The positive anomaly at the 8°N trough combined with the negative anomaly at the 4°N crest reduce the tilt at the position of the NECC that marks a decrease of the strength of the current. This is confirmed by the surface current differences in Fig. 6b that show westward anomalies in the NECC. Similarly, the two lobes mark a reduction of the meridional tilt of the isocontours along the equator that indicates a decrease of the SEC intensity in the equatorial band. In the western boundary, the important decrease of the SSH should result in a reduction of the equatorward western boundary currents.
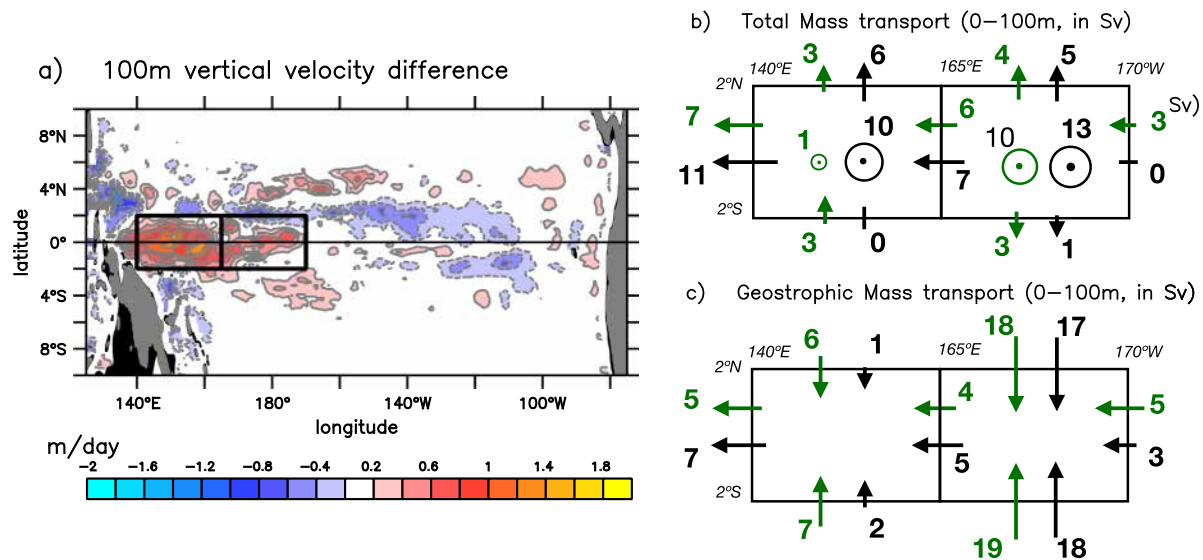
8

Fig. 5. (a) Map of AssimALL-minus-AssimTS differences of the vertical velocity (m/day) at 100 m time-averaged over the 2008–2014 period. (b) Total mass transport (10^{-6}m³/s, Sv) in the upper 100 m in the western equatorial Pacific for AssimTS (green arrows) and AssimALL (black arrows) in the two boxes in (a). (c) Same as (b) except for the geostrophic component.

Given that the difference of the steric height at the surface relative to 300 m (0/300 SH) between AssimALL and AssimTS in Fig. 6b shows similar patterns to that based on SSH (Fig. 6a), previous conclusions at the surface changes can be extended in subsurface. Note that the SH, as the baroclinic component of the sea level, is deduced from the density field and is integrative view of the thermohaline stratification. Similar patterns are seen on the difference of steric height at 100 m relative to 300 m between the two simulations (in Fig. 6c), indicating that SSH differences reflect modifications of the subsurface stratification. The close relationship of the 100-m current anomalies with differences of the steric height at 100 m clearly indicates that the horizontal current differences are mainly driven by the changes of the pressure gradient. Additionally, the equatorward western boundary circulation is significantly reduced. At 3.5°S, the northward mass transport in the 0–700 m layer from the western boundary to 170°E is reduced from 14.2 Sv in AssimTS to 9.8 Sv in AssimALL. Note that the mass transport at the entrance of the Solomon sea is estimated at 15 Sv from repeated glider transects (Davis et al., 2012). All these modifications mainly driven by SSH changes are expected to act on the large-scale circulation in modifying the mass transport from the Pacific to the Indian oceans through the Indonesian Throughflow (Kamenkovich et al., 2003). This would require further investigations.

4.3. Zonal pressure gradient and the mean dynamic topography

Here we focus on the different features of the zonal pressure gradient. Several studies have shown that the zonal pressure gradient can be closely related to the zonal slope of the SSH (e.g., Nagura and McPhaden, 2008). Consequently, in modifying the mean SSH, the assimilation of altimetry by the addition of a MDT can potentially impact on the mean pressure gradient. Here, we only consider changes of the zonal pressure gradient, but similar conclusions can be made in the meridional direction.

The vertical structure of the mean zonal pressure gradient is presented in Fig. 7 (lower panels). In general, the shape and amplitude of the zonal pressure gradient are consistent from that reported by historical studies (Mangum and Hayes, 1984; Qiao and Weisberg, 1997; Yu and McPhaden, 1999). A zonal pattern is found in the two solutions, with a weaker amplitude west of 170°E than in the central-eastern Pacific, consistently with a weaker mean surface wind stress in the west (Yu and McPhaden, 1999). In the central-eastern Pacific, the zonal

pressure gradient is clearly eastward above the thermocline, with a maximum in the central Pacific ($>5 \times 10^{-7}$m/s²). The AssimALL-minus-AssimTS difference (Fig. 7c) indicates a large-scale pattern, with a significant negative anomaly (-2×10^{-7} m/s²) in the western Pacific, and to a lesser extent in the far eastern Pacific.

To understand the relationship of the zonal pressure gradient with the zonal gradient of SSH as identified in several studies (Yu and McPhaden, 1999; Nagura and McPhaden, 2008), the zonal pressure gradient is vertically integrated in Fig. 7 (upper panels). As mentioned previously, a minimum is found in the western Pacific and a maximum in the central Pacific. Looking specifically at the differences between AssimALL and AssimTS (Fig. 7c), changes of -2×10^{-5} m²/s² in the depth-integrated zonal pressure gradient in the western Pacific correspond to changes of -2×10^{-7} m/s² in the zonal gradient of the SSH. In that region, variations of the zonal pressure gradient are large (Yu and McPhaden, 1999), and the amplitude of the AssimALL-minus-AssimTS difference is comparable to the magnitude of the variability occurring at seasonal to interannual time scales (Yu and McPhaden, 1999).

Since an important difference between the AssimTS and the AssimALL solutions is the assimilation of the SSH anomaly provided by altimetry (only assimilated in AssimALL), a question is whether the use of a MDT to convert the model SSH in sea level anomaly (SLA) such as $SLA = SSH - MDT$ can generate large-scale patterns in the zonal pressure gradient. To address this question, the 0/300 steric height (0/300 SH) is computed from AssimTS and AssimALL temperature and salinity fields and compared with that computed from TAO/TRITON temperature combined with Argo salinity (Fig. 8a). Errors due to gaps in TAO/TRITON time series, based on the difference between the mean 0/300 SH from the complete AssimALL fields and that from fields co-located in time with the TAO/TRITON moorings, are not significant (lower than 1 cm, not shown).

The 0/300 SH in the AssimTS (and NoAssim) is closer to observations than that in the AssimALL in the western Pacific, with differences reaching 7 cm at 137°E. To determine if the MDT can be related with the SH discrepancy, the MDT for the assimilation of altimetry in AssimALL is shown in Fig. 8, as well as the main components used in the MDT computation; the observation-based CNES-CLS13 MDT and the model MDT (see Hamon et al., 2019). As each MDT is computed over a different period, the sea level anomaly from the gridded DUACS product averaged over the time-period of each MDT has been removed from each estimate to remove the effects of the long-term
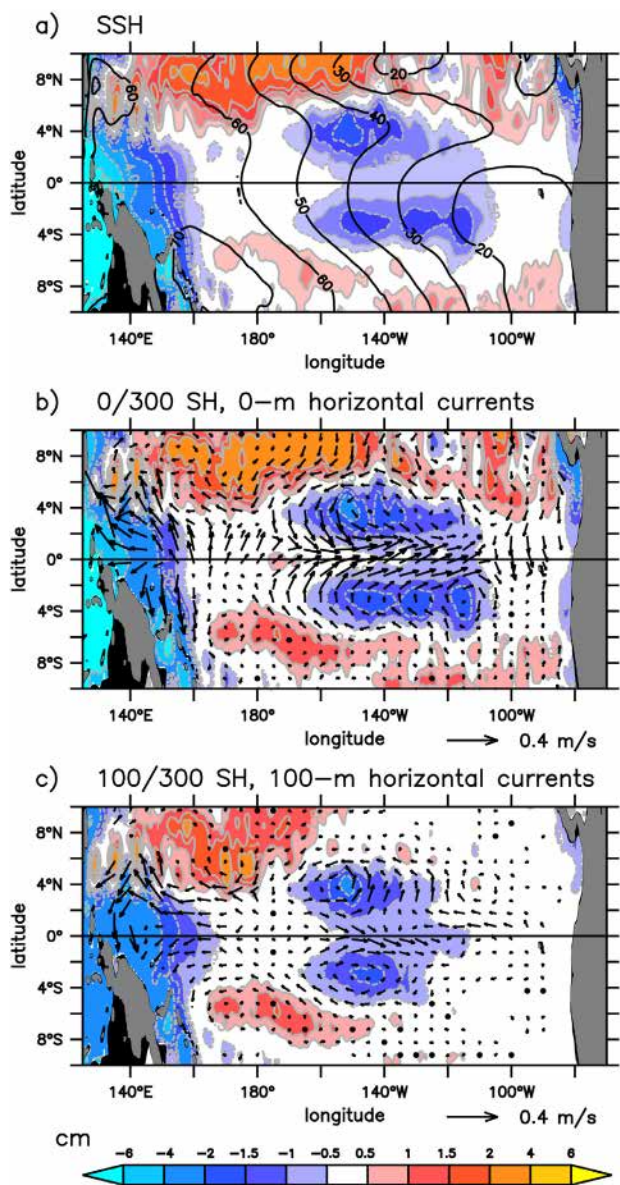
Fig. 6. (a) Map of the 2008–2014 mean of the AssimALL SSH (contour, in cm) and the difference from AssimTS (shading). (b) Map of the steric height difference (AssimALL-minus-AssimTS) at the surface relative to 300 m (0/300 SH, shading, in cm) , and surface horizontal currents (arrows). (c) Same as (b) except for the 100 m surface (100/300 SH).

Fig. 7. Equatorial sections of the 2008–2014 mean of the zonal pressure gradient $(-\langle P_x \rangle / \rho_0)$ referenced at 300 m ((lower panels) vertical structure in 10^{-7} m/s^2, (upper panels) vertically integrated in 10^{-5} m^2/s^2) from AssimTS, AssimALL and AssimALL-minus-AssimTS difference (black lines). For comparison, the zonal gradient of SSH $(-gSSH_x$, in 10^{-7} m/s^2) is shown in the upper panels (red lines).

variability. It shows that the zonal pattern of the CNES-CLS13 MDT, similar to that of the latest version CNES-CLS18 MDT, has a zonal slope that is more consistent with the slope of the TAO/TRITON 0/300 SH than the MDT used in AssimALL (Fig. 8b). This suggests that the CNES-CLS MDT is not responsible for the pattern of the MDT used in AssimALL. The strong zonal slope of the MDT used in AssimALL mostly seen west of 160°E is rather due to the model MDT from the previous reanalysis (GLORYS2V3) (Fig. 8c, see Section 2.1). Such MDT biases in the western Pacific, not sufficiently corrected during the MDT procedures (Hamon et al., 2019), have important and problematic consequences for the physical–BGC model. Consequently, the computation of the MDT should be reevaluated with regards to these results. However, it is important to mention that obtaining a global accurate MDT resolving simultaneously equatorial regions, high latitudes plus continental shelves are far to be straightforward, and has rather to be seen as a long-term process.
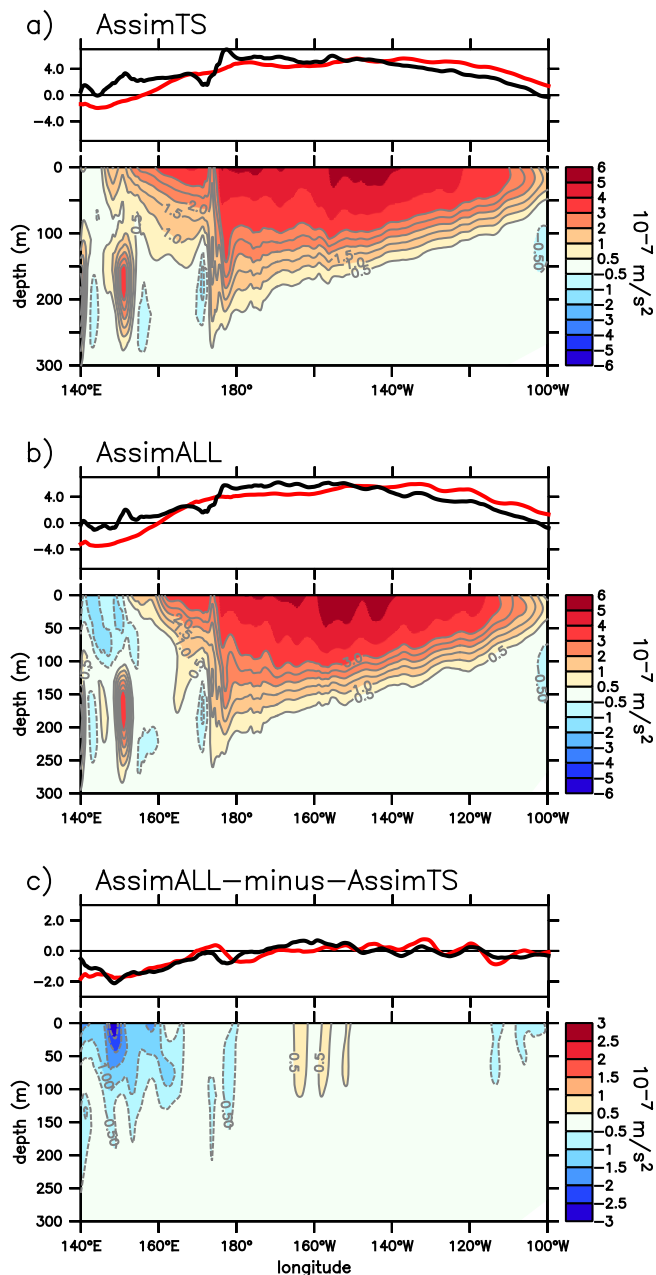
As will be shown, the comparison of surface chlorophyll in the tropical Pacific and nitrate concentration along the equatorial Pacific shows that modified MDT strongly reduces differences from observations demonstrating that differences between AssimTS and AssimALL are mostly due to biases in the MDT.

4.4. Impact of altimetry assimilation with dedicated experiments

As mentioned in Section 2, differences between AssimALL and AssimTS are due to the assimilation of altimetry and the use of the SEEK filter. The comparison of NOALTI with the CONTROL experiment allows to assess the sensitivity of the system due to the assimilation of altimetry (the SEEK filter is used for in situ observations), while
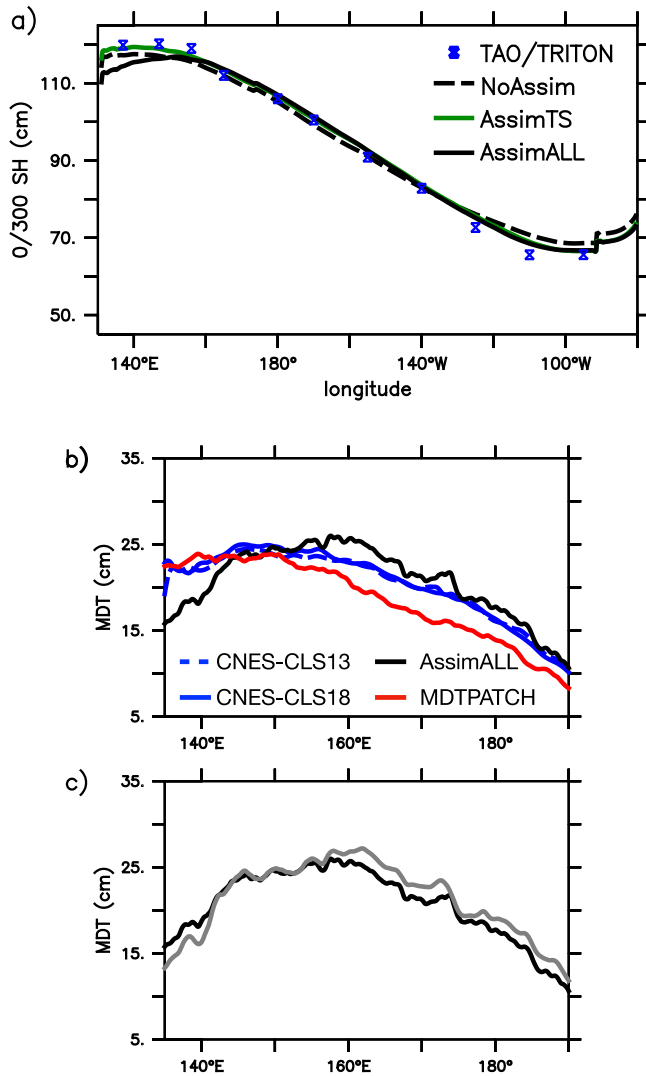
Fig. 8. (a) 0/300 steric height along the equator from TAO/TRITON estimates (blue crosses), and NoAssim, AssimTS, and AssimALL (respectively, dashed black, green, full black). (b) MDT used for altimetry assimilation in AssimALL (black), the observation-only MDTs, CNES-CLS13 and CNES-CLS18, and the MDT used in the MDTPATCH experiment. (c) MDT used for altimetry assimilation in AssimALL (black) and the MDT model (gray line) which has been used for its computation.

Fig. 9. Bin-averaged residuals (1° × 1°, analysis-minus-observations) of sea level anomaly computed over the period June 2014–May 2015 from (a) the CONTROL and (b) the MDTPATCH experiments. The analyzed sea level anomaly is computed as the sea surface height minus the MDT. Note that the bin-averaged residuals from the CONTROL experiment have been added to the MDT used in MDTPATCH.

the comparison with MDTPATCH demonstrates the sensitivity due to the MDT. In MDTPATCH, the modified MDT (>5 cm along the equator around 165°E) has been built from the SLA residuals of the CONTROL run corresponding to the differences of the observed SLA and the analyzed SLA (i.e, model sea surface height minus the MDT) which have been bin-averaged for the period June 2014–May 2015 (Fig. 9). Note that the zonal slope is strongly reduced (Fig. 8c).

In Fig. 10a,b, a significant reduction of the vertical velocity (∼0.5 m/day) is seen in the western equatorial Pacific on both MDT-PATCH and NOALTI experiments. This is associated with a reduction of the cold bias seen in the CONTROL run (∼0.5 °C, Fig. 10c). This supports the key role of the MDT in the Mercator Ocean system in triggering biases in equatorial physics. Note that reduction of the warm bias in the eastern Pacific, especially in NOALTI, might reflect an inconsistency between satellite and in situ observations, and this deserves to be further investigated later on. In Fig. 11, BGC fields forced by the CONTROL run shows similar differences from observations than that forced with AssimALL (Fig. 1). The western Pacific is strongly productive with high concentration of surface Chl and nitrates. Compared with the CONTROL run, BGC fields forced by MDTPATCH and NOALTI
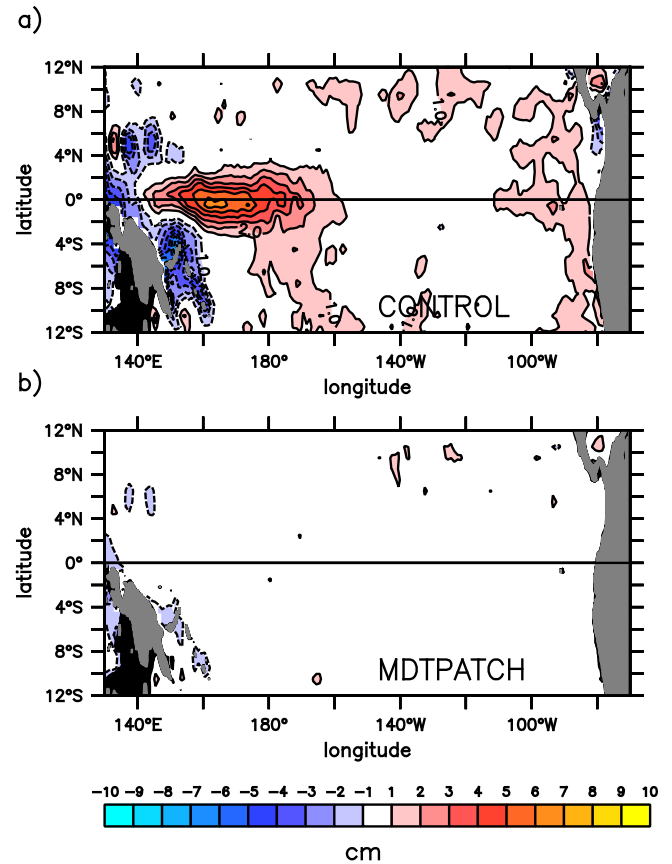
have smaller differences with observations, demonstrating the key role of the MDT used for the assimilation procedures of altimetry in the issues seen in the tropical Pacific physics and biogeochemistry in the Mercator Ocean system.

5. Interpretation of the temperature balance

Having revealed the mechanisms that lead to an increase in the vertical velocity in the western Pacific due to the assimilation of altimetry, we discuss the consequences of such modifications in terms of the heat balance. In the mean, the significant amplification of equatorial upwelling in the western Pacific bringing cold deep waters in the surface layer raises the question of the heat balance, especially with regards to the strong cold anomaly found in AssimALL in the western Pacific around 150 m (Fig. 4a).

$$\partial_t \langle T \rangle = \underbrace{-\langle u\partial_x T \rangle - \langle v\partial_y T \rangle - \langle w\partial_z T \rangle}_{Adv} + \underbrace{\frac{Q_{net}}{\rho_0 C_p H}}_{HF} + \underbrace{\langle Inc_T \rangle}_{Inc} + R \qquad (2)$$

where the angle brackets denote the depth integration over the upper 300 m. Adv represents the advection term, HF is the net heat flux with ρ_0 the density of sea water (1025 kg/m^3) and C_p the heat capacity (3940 J/kg/°C), Inc is the temperature increment (correction to apply to the model) due to data assimilation (In AssimTS, the increment is only a large-scale temperature correction, while in AssimALL the temperature increment is the weighted sum of the large-scale temperature one and the small-scale one coming from the multivariate SEEK filter).
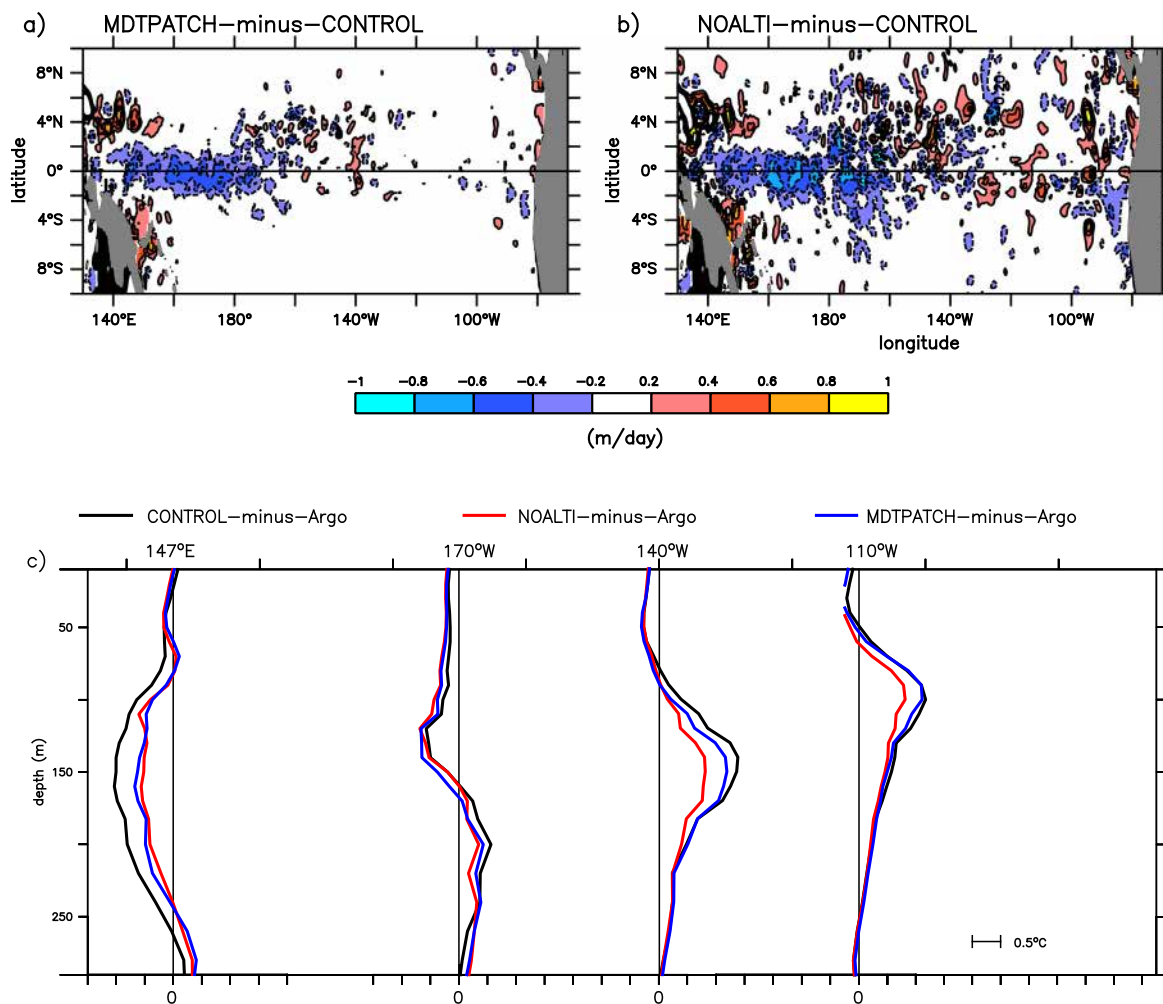
Fig. 10. (a–b) Vertical velocity difference at 100 m from the CONTROL experiment for (a) MDTPATCH and (b) NOALTI experiments. (c) Same as Fig. 4a (temperature differences from Argo), but for the CONTROL, MDTPATCH and NOALTI experiment. Temperature differences from Argo have been computed over the period June 2014–May 2015.

The term R is a residual, which includes entrainment, horizontal and vertical mixing.

To understand the role of data assimilation on the mean heat balance, the mean temperature increments averaged in the 0–300 m layer from the AssimTS and AssimALL simulations are shown in Fig. 12. On average, data assimilation slightly cools the eastern equatorial Pacific in AssimTS. Compared to AssimTS, the mean temperature increment in AssimALL is much stronger and the pattern is a dipole with a significant warming west of the dateline and cooling east of it. The magnitude of the warming reaches 1 °C/month in the far western Pacific.

The sum of the advection and heat flux terms are shown in Fig. 12b,d. While the net heat flux contribution mainly results from the atmospheric forcing, the advection term is obtained by computing monthly averages of each component of term (A) in Eq. (2) from daily fields of temperature and velocity. The clear correspondence between Fig. 12c and d, but with opposite sign, indicates that mean temperature increment is related with the net heat flux and advection terms. While the surface heat flux is almost unchanged, the contribution of advection is determinant in controlling temperature increments. Actually most of heat advection in AssimALL is due to the vertical component (not shown). For comparison, the mean net heat flux in the Niño 3 box [150°W–90°W; 5°S–5°N] is lower than 0.2 °C/mon indicating that the warming applied by data assimilation is huge with regards to the mean heat balance.

Given the magnitude of the mean temperature increments compared to the net heat flux, we now consider the long term evolution

of the ocean heat content. Long term changes of steric height from data assimilation systems can be inconsistent with observation-based estimates (Storto et al., 2018; Gasparin et al., 2018). The ocean heat content (OHC) evolution is computed from $OHC = \rho_0 C_p \int_{-300m}^{0} T' dz$ with T' the anomaly from the 2008–2014 mean. Fig. 13a shows the ocean heat content integrated in the tropical Pacific [170°E–100°W; 12°S–12°N] from the SCRIPPS Argo product, AssimTS and AssimALL estimates. While AssimTS is in agreement with Argo (0.14 10^{22} J/yr), the OHC from AssimALL is two times higher (0.29 10^{22} J/yr).

Finally, to evaluate the possibility that changing the mean heat balance might induce a spurious ocean heat gain, the AssimALL-minus-AssimTS OHC difference only based on temperature fields is compared with OHC differences from reconstructed time series by integrating the sum of the advection, net heat flux and temperature increment terms. This comparison demonstrates that the modification of the mean heat balance by inconsistent mean temperature increment likely results in a higher mean local warming.

6. Conclusion and discussion

The general framework of this study is a well-known persistent problem in physical–BGC models, regarding an unrealistic Chl surface concentration and an unrealistic accumulation of nitrates in the tropical Pacific when forced by outputs from physical reanalyses. Given the strong sensitivity of BGC models to the physical forcing in that region, the present study has assessed the consequences of physical data assimilation on the representation of the mean dynamics from a set of three
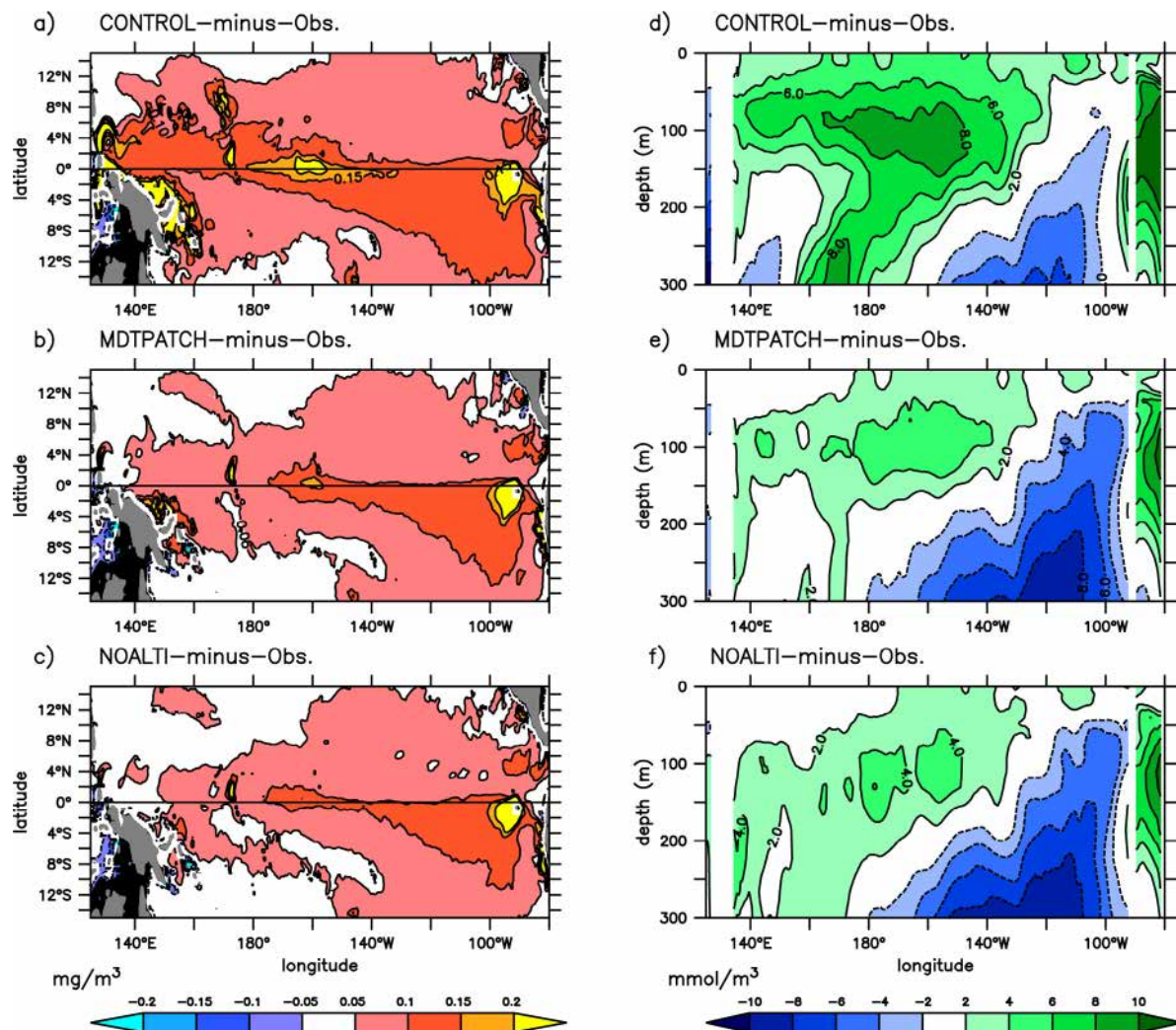
Fig. 11. Same as Fig. 1 (surface Chl (a–c) and equatorial nitrate (d–f) concentrations), except for the CONTROL, MDTPATCH and NOALTI experiments. Differences have been computed over the period June 2014–May 2015. Note that unlike Fig. 1, only differences from observations are shown.

sister ocean reanalysis runs that use the same physical–BGC model configuration but that differ in their level of physical data assimilation. Based on a series of simple cause–effect mechanisms, it is shown that the sensitivity of the BGC model in the tropical Pacific to physical data assimilation is mainly related to important differences in the intensity of the mean equatorial upwelling in the western equatorial Pacific resulting from changes in the pressure field. The western tropical Pacific has a key role in the dynamics of the whole tropical Pacific in our physical–BGC model, consistently with results from the seasonal forecasting system at ECMWF (Balmaseda and Anderson, 2009).

Based on the analysis of the nitrate budget in the equatorial euphotic layer, the simulation having both levels of data assimilation (AssimALL; a 3D-Var large-scale T/S correction and a multivariate correction applied on the prognostic variables from the SEEK filter) is mainly characterized by an unrealistic vertical advection flux of nitrates in the western Pacific. These nitrates are then distributed along the whole equatorial basin by the horizontal circulation. Nearly all the excess of nitrates is consumed through biological processes that explain the higher Chl concentrations at the sea surface. Additionally, as the vertical input of nitrates is not totally compensated by the consumption of biological processes, small positive residuals cause a long-term accumulation of nitrates in the tropical band. Moreover, the analysis of the vertical velocity reveals that changes in the vertical advection flux is driven by the mean value rather than the small scale variability associated with potential assimilation shocks. The signature

of the enhanced upwelling in the western equatorial Pacific is seen in vertical sections of the thermal stratification and currents with an upward displacement of the isolines.

Resulting by definition from the continuity equation, the changes of the vertical velocity reflect the modifications of the zonal and meridional circulations. We point out that biases in the MDT required for referencing the sea level anomaly provided by altimetry have strong impacts on the tropical circulation in the whole basin. In modifying the mean SSH, the MDT changes the subsurface pressure field associated with the thermohaline stratification. Additionally, these biases of the MDT lead to an unrealistic long-term ocean warming in the tropical Pacific. In fact, the vertical flux of cold water due to the increased upwelling in the western Pacific induces a strong temperature increment (reaching 1 °C/mon) equivalent to five times the surface heat flux. However, the upwelled cold water and the warm increments are not totally balanced, causing a local heat excess in the whole tropical basin.

The assimilation of altimetric sea level anomaly is important for representing key mechanisms for biogeochemistry in the equatorial Pacific such as tropical instability waves (e.g., Gorgues et al., 2005). Further investigations are thus needed to refine the MDT. It may be tempting to apply a correction patch based on the mean difference between altimetry and the model (as done in the experiments), but ocean reanalyses are based on atmospheric forcing, model processes
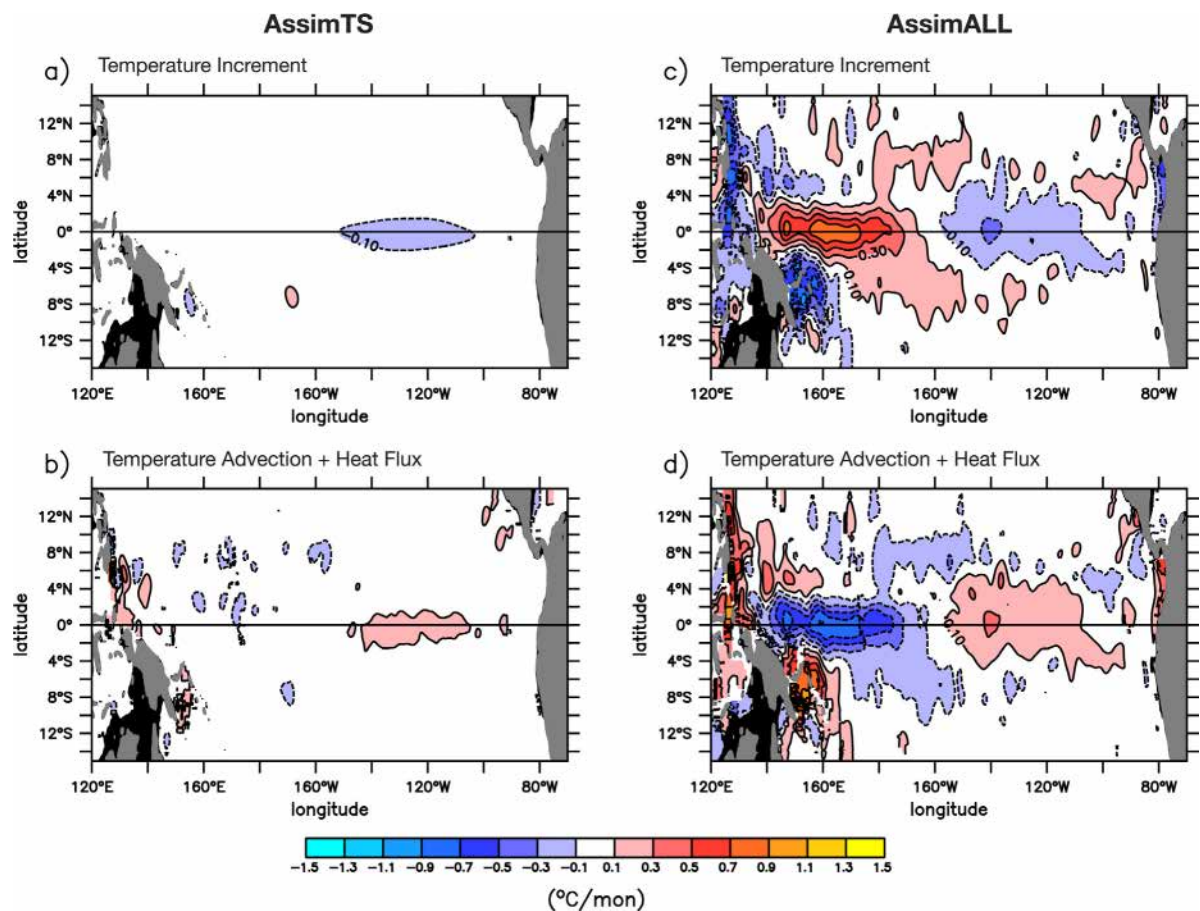
Fig. 12. (a) Mean temperature increment averaged in the 0–300 m layer and (b) the mean advection and heat flux terms of Eq. (2) from AssimTS. (c,d) Same as (a,b) except for AssimALL.

and data assimilation, with errors in surface forcing and modeled processes compensated by data assimilation. In constraining thermohaline stratification and SSH, data assimilation modifies one of the components of this balance, without significantly changing the net surface forcing (wind stress, heat and freshwater fluxes), resulting in disturbing the initial balance. However, the temptation to artificially modify one of the components of the system toward keeping some theoretical balance can be counterproductive given the continuous evolution of the elements of the system.

Several improvements of the MDT computation and of the assimilation techniques are expected to improve the general balance. As the computation of the MDT combines satellites and in situ measurements, its local accuracy depends on the evolution of the global ocean observing system. While the advent gravimetric data have improved our knowledge of the Earth's geoid (Castruccio et al., 2008; Rio et al., 2013), more advanced techniques will increase the resolution of the MDT and include more accurate details of the ocean circulation (Knudsen et al., 2019). Additionally, enhancing in situ measurements are also essential for refining the accuracy of the MDT (Rio et al., 2011). While the first deployments of Argo floats with Argos antenna were strongly sensitive to the equatorial divergence (Gasparin et al., 2015), recent deployments of floats equipped with Iridium antenna may be of great interest. Although the accuracy of the MDT will progress over time, this study demonstrates that error statistics of the MDT is important for operational systems. As mentioned in Section 2.1, the MDT and SLA errors are estimated by the Desroziers method at a scale of about 150 km, which is consistent with altimetric information. However, Fig. 8 shows that there is larger scale bias (of the order of 10° of longitude) which is not considered in the current approach. Further work is needed to estimate the error and bias jointly, rather than using the Desroziers non-bias hypothesis.

This analysis ends up pointing out the key role of the MDT during the assimilation procedures of altimetry in the Mercator Ocean system. However, it is important to mention that our conclusions do not hold in other operational systems assimilating only T/S profiles with similar issues (While et al., 2010; Park et al., 2018b). The question of why the issue is not seen in AssimTS is a reasonable one. We argue that, by introducing a supplementary force in the prognostic model equations, the IAU reduces the imbalance between the pressure gradient force and the atmospheric forcing, as shown in the North Atlantic due to an initial MDT bias lower than 2 cm (Benkiran and Greiner, 2008; While et al., 2010). Thus, this study demonstrates that the IAU is not sufficient in the tropical Pacific where the MDT bias can reach 7 cm over more than 3000 km. However, we hope that our study will stimulate other careful diagnostics of the physics to help better understand the causes of the vertical velocity biases that may differ from the Mercator Ocean system. As demonstrated here, this goes through a better understanding of the physics and biogeochemistry in the equatorial Pacific and in situ observations from the Tropical Pacific Observing System (TPOS) will strongly contribute to it.

Several follow-on aspects of TPOS that are fundamental for physical–BGC models are pointed out by the present study. Velocity measurements in the surface and subsurface layers are unique information for data assimilation systems because they are not assimilated and constitute independent data sets for assessing and improving the representation of the ocean circulation by physical models. BGC measurements along the water column from Argo floats are also strongly required to evaluate, improve, and eventually, assimilate it into models. While the ocean color dataset is commonly assimilated in BGC models (Ford et al., 2018), significant work is needed for assimilating BGC floats.

Our objective has been to quantitatively assess the capabilities of the physical–BGC model in the tropical Pacific, and to provide some
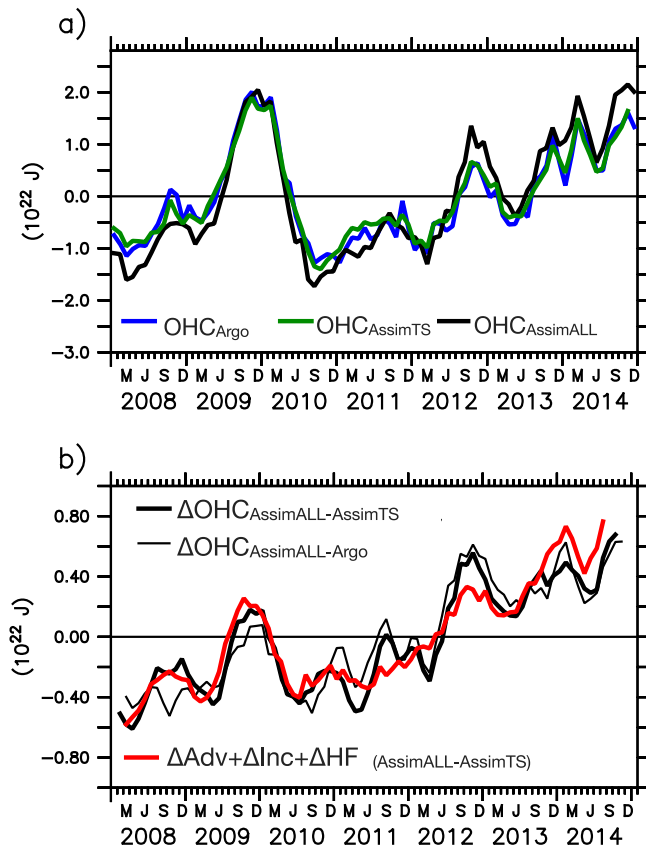
Fig. 13. (a) Time series of ocean heat content (OHC, 0–300 m) in the central-eastern tropical Pacific, 170E–100 W, 12S–12N) from Argo, AssimTS and AssimALL solutions deduced from the sum of the time-integrated advection and incremental terms of Eq. (2). (b) OHC differences between AssimALL and AssimTS (thick black line), and AssimALL and Argo (thin black line) from (a) in black, and reconstructed by time-integration of the sum of advection, net heat flux and incremental terms of Eq. (2) in red. For comparison, AssimALL-minus-Argo is shown in thin black line.

elements to the evolving design of the TPOS (Smith et al., 2019). This integrated vision from physical–BGC models illustrates that the contribution of ocean observations for ocean models should thus be evaluated by its direct impact on systems evaluation and data assimilation, but also by its indirect impact through the MDT, that can be equivalent (Balmaseda and Anderson, 2009). Finally, this study demonstrates that looking into details of the physics is indispensable to improve physical data assimilation systems, to better understand their relationship with BGC models and to ensure that they make the best use of oceanic observations.

CRediT authorship contribution statement

Florent Gasparin: Conceptualization, Writing - original draft. **Sophie Cravatte:** Writing - review & editing. **Eric Greiner:** Writing - review & editing. **Coralie Perruche:** Methodology. **Mathieu Hamon:** Methodology. **Simon Van Gennip:** Writing - review & editing. **Jean-Michel Lellouche:** Methodology, Writing - review & editing.

Declaration of competing interest

The authors declare that they have no known competing financial interests or personal relationships that could have appeared to influence the work reported in this paper.

Appendix A. Supplementary data

Supplementary material related to this article can be found online at https://doi.org/10.1016/j.ocemod.2021.101768.

References

Aumont, O., Éthé, A., Bopp, L., Gehlen, M., 2015. PISCES-v2: an ocean biogeochemical model for carbon and ecosystem studies. Geosci. Model Dev. Discuss. 8.

Aumont, O., Orr, J.C., Jamous, D., Monfray, P., Marti, O., Madec, G., 1998. A degradation approach to accelerate simulations to steady-state in a 3-D tracer transport model of the global ocean. Clim. Dynam. 14, 101–116. http://dx.doi.org/10.1007/s003820050212.

Balmaseda, M., Anderson, D., 2009. Impact of initialization strategies and observations on seasonal forecast skill. Geophys. Res. Lett. (36), http://dx.doi.org/10.1029/2008GL035561.

Bell, M.J., Martin, M.J., Nichols, N.K., 2004. Assimilation of data into an ocean model with systematic errors near the equator. Q. J. R. Meteorol. Soc.: A J. Atmos. Sci. Appl. Meteorol. Phys. Oceanogr. 130, 873–893.

Benkiran, M., Greiner, E., 2008. Impact of the incremental analysis updates on a real-time system of the North Atlantic Ocean. J. Atmos. Ocean. Technol. 25, 2055–2073.

Berthet, S., Séférian, R., Bricaud, C., Chevallier, M., Voldoire, A., Ethé, C., 2019. Evaluation of an online grid-coarsening algorithm in a global eddy-admitting ocean biogeochemical model. J. Adv. Modelling Earth Syst. 11, 1759–1783. http://dx.doi.org/10.1029/2019MS001644.

Birol, F., Brankart, J.M., Castruccio, F., Brasseur, P., Verron, J., 2004. Impact of ocean mean dynamic topography on satellite data assimilation. Mar. Geodesy 27, 59–78.

Bloom, S.C., Takacs, L.L., Da Silva, A.M., Ledvina, D., 1996. Data assimilation using incremental analysis updates. Mon. Weather Rev. 124, 1256–1271.

Brasseur, P., Verron, J., 2006. The SEEK filter method for data assimilation in oceanography: a synthesis. Ocean Dyn. 56, 650–661.

Burgers, G., Balmaseda, M.A., Vossepoel, F.C., van Oldenborgh, G.J., Van Leeuwen, P.J., 2002. Balanced ocean-data assimilation near the equator. J. Phys. Oceanogr. 32, 2509–2519.

Cabanes, C., Grouazel, A., von Schuckmann, K., Hamon, M., Turpin, V., Coatanoan, C., Paris, F., Guinehut, S., Boone, C., Ferry, N., de Boyer Montégut, C., Carval, T., Reverdin, G., Pouliquen, S., Le Traon, P.Y., 2013. The CORA dataset: validation and diagnostics of in-situ ocean temperature and salinity measurements. Ocean Sci. 9, 1–18. http://dx.doi.org/10.5194/os-9-1-2013.

Castruccio, F., Verron, J., Gourdeau, L., Brankart, J.M., Brasseur, P., 2008. Joint altimetric and in-situ data assimilation using the GRACE mean dynamic topography: a 1993–1998 hindcast experiment in the Tropical Pacific ocean. Ocean Dyn. 58, 43–63.

Chen, D., Smith, N., Kessler, W., 2018. The evolving ENSO observing system. Nat. Sci. Rev. 5, 805–807.

Davis, R.E., Kessler, W.S., Sherman, J.T., 2012. Gliders measure western boundary current transport from the south Pacific to the equator. J. Phys. Oceanogr. 42, 2001–2013. http://dx.doi.org/10.1175/JPO-D-12-022.1.

Desroziers, G., Berre, L., Chapnik, B., Poli, P., 2005. Diagnosis of observation, background and analysis-error statistics in observation space. Q. J. R. Meteorol. Soc. A J. Atmos. Sci. Appl. Meteorol. Phys. Oceanogr. 131, 3385–3396, Publisher: Wiley Online Library.

Donlon, C.J., Martin, M., Stark, J., Roberts-Jones, J., Fiedler, E., Wimmer, W., 2012. The operational sea surface temperature and sea ice analysis (OSTIA) system. Remote Sens. Environ. 116, 140–158. http://dx.doi.org/10.1016/j.rse.2010.10.017.

Feely, R.A., Wanninkhof, R., Cosca, C.E., Murphy, P.P., Lamb, M.F., Steckley, M.D., 1995. CO2 distributions in the equatorial Pacific during the 1991–1992 ENSO event. Deep Sea Res. Part II: Top. Stud. Oceanogr. 42, 365–386.

Fennel, K., Gehlen, M., Brasseur, P., Brown, C.W., Ciavatta, S., Cossarini, G., Crise, A., Edwards, C.A., Ford, D., Friedrichs, M.A.M., Gregoire, M., Jones, E., Kim, H.C., Lamouroux, J., Murtugudde, R., Perruche, C., 2019. Advancing marine biogeochemical and ecosystem reanalyses and forecasts as tools for monitoring and managing ecosystem health. Front. Mar. Sci. (6), http://dx.doi.org/10.3389/fmars.2019.00089.

Ford, D., Key, S., McEwan, R., Totterdell, I., Gehlen, M., 2018. Marine biogeochemical modelling and data assimilation for operational forecasting, reanalysis, and climate research. New Front. Oper. Oceanogr. 625–652.

Fujii, Y., Cummings, J., Xue, Y., Schiller, A., Lee, T., Balmaseda, M.A., Rémy, E., Masuda, S., Brassington, G., Alves, O., Cornuelle, B., Martin, M., Oke, P., Smith, G., Yang, X., 2015. Evaluation of the Tropical Pacific Observing System from the ocean data assimilation perspective. Q. J. R. Meteorol. Soc. 141, 2481–2496. http://dx.doi.org/10.1002/qj.2579.

Garcia, H.E., Locarnini, R.A., Boyer, T.P., Antonov, J.I., Baranova, O.K., Zweng, M.M., Reagan, J.R., Johnson, D.R., Mishonov, A.V., Levitus, S., 2013. World ocean atlas 2013. In: Volume 4, Dissolved Inorganic Nutrients (Phosphate, Nitrate, Silicate).

Garcia, H.E., Weathers, K., Paver, C.R., Smolyar, I., Boyer, T.P., Locarnini, R.A., Zweng, M.M., Mishonov, A.V., Baranova, O.K., Seidov, D., Reagan, J.R., 2018. World ocean atlas 2018. In: Garcia, H.E. K., Weathers, C.R., Paver, I., Smolyar, T.P., Boyer, R.A., Locarnini, M.M., Zweng, A.V., Mishonov, O.K., Baranova, D., Seidov, Reagan, J.R. (Eds.), Volume 4: Dissolved Inorganic Nutrients (Phosphate, Nitrate and Nitrate+Nitrite, Silicate). p. 35.

Garnesson, P., Mangin, A., Fanton d'Andon, O., Demaria, J., Bretagnon, M., 2019. The CMEMS GlobColour chlorophyll *a* product based on satellite observation: multi-sensor merging and flagging strategies. Ocean Science 15, 819–830. http://dx.doi.org/10.5194/os-15-819-2019.

Gasparin, F., Greiner, E., Lellouche, J.M., Legalloudec, O., Garric, G., Drillet, Y., Bourdallé-Badie, R., Le Traon, P.Y., Rémy, E., Drévillon, M., 2018. A large-scale view of oceanic variability from 2007 to 2015 in the global high resolution monitoring and forecasting system at Mercator Océn. J. Mar. Syst. 187, 260–276.

Gasparin, F., Roemmich, D., Gilson, J., Cornuelle, B., 2015. Assessment of the upper-ocean observing system in the equatorial Pacific: The role of argo in resolving intraseasonal to interannual variability. J. Atmos. Ocean. Technol. http://dx.doi.org/10.1175/JTECH-D-14-00218.1.

Good, S.A., Martin, M.J., Rayner, N.A., 2013. EN4: Quality controlled ocean temperature and salinity profiles and monthly objective analyses with uncertainty estimates. J. Geophys. Res. Oceans 118, 6704–6716.

Gorgues, T., Menkes, C., Aumont, O., Vialard, J., Dandonneau, Y., Bopp, L., 2005. Biogeochemical impact of tropical instability waves in the equatorial Pacific. Geophys. Res. Lett. 32. http://dx.doi.org/10.1029/2005GL024110, https://agupubs.onlinelibrary.wiley.com/doi/abs/10.1029/2005GL024110, _eprint: https://agupubs.onlinelibrary.wiley.com/doi/pdf/10.1029/2005GL024110.

Guiavarc'h, C., Roberts-Jones, J., Harris, C., Lea, D.J., Ryan, A., Ascione, I., 2019. Assessment of ocean analysis and forecast from an atmosphere–ocean coupled data assimilation operational system. Ocean Sci. (15).

Guilyardi, E., Wittenberg, A., Balmaseda, M., Cai, W., Collins, M., McPhaden, M.J., Watanabe, M., Yeh, S.W., 2016. Fourth CLIVAR workshop on the evaluation of ENSO processes in climate models: ENSO in a changing climate. Bull. Amer. Meteorol. Soc. 97, 817–820.

Hamon, M., Greiner, E., Le Traon, P.Y., Remy, E., 2019. Impact of multiple altimeter data and mean dynamic topography in a global analysis and forecasting system. J. Atmos. Ocean. Technol. 36, 1255–1266. http://dx.doi.org/10.1175/JTECH-D-18-0236.1.

Ishii, M., Feely, R.A., Rodgers, K.B., Park, G.H., Wanninkhof, R., Sasano, D., Sugimoto, H., Cosca, C.E., Nakaoka, S.i., Telszewski, M., 2014. Air-sea CO2 flux in the Pacific ocean for the period 1990-2009. Biogeosciences 11, 709–734, Publisher: European Geosciences Union.

Johnson, G.C., Sloyan, B.M., Kessler, W.S., McTaggart, K.E., 2002. Direct measurements of upper ocean currents and water properties across the tropical Pacific during the 1990s. Prog. Oceanogr. 52, 31–61.

Kamenkovich, V., Burnett, W., Gordon, A., Mellor, G., 2003. The Pacific/Indian Ocean pressure difference and its influence on the Indonesian Seas circulation: Part II—The study with specified sea-surface heights. J. Mar. Res. (61), http://dx.doi.org/10.1357/002224003771815972.

Knudsen, P., Andersen, O., Maximenko, N., 2019. A new ocean mean dynamic topography model, derived from a combination of gravity, altimetry and drifter velocity data. Adv. Space Res. http://dx.doi.org/10.1016/j.asr.2019.12.001.

Lauvset, S.K., Key, R.M., Olsen, A., van Heuven, S., Velo, A., Lin, X., Schirnick, C., Kozyr, A., Tanhua, T., Hoppema, M., 2016. A new global interior ocean mapped climatology: The 1× 1 GLODAP version 2. Earth Syst. Sci. Data 8, 325–340.

Lea, D.J., Drecourt, J.P., Haines, K., Martin, M.J., 2008. Ocean altimeter assimilation with observational-and model-bias correction. Q. J. R. Meteorol. Soc. 134, 1761–1774, Publisher: Wiley Online Library.

Lellouche, J.M., Greiner, E., Le Galloudec, O., Garric, G., Regnier, C., Drevillon, M., Benkiran, M., Testut, C.E., Bourdalle-Badie, R., Gasparin, F., Hernandez, O., Levier, B., Drillet, Y., Remy, E., Le Traon, P.Y., 2018. Recent updates on the copernicus marine service global ocean monitoring and forecasting real-time 1/12 high resolution system. Ocean Sci. Discuss 2018, 1–70. http://dx.doi.org/10.5194/os-2018-15.

Lellouche, J.M., Le Galloudec, O., Drévillon, M., Régnier, C., Greiner, E., Garric, G., Ferry, N., Desportes, C., Testut, C.E., Bricaud, C., et al., 2013. Evaluation of global monitoring and forecasting systems at Mercator Océn. Ocean Sci. 9 (57).

Locarnini, R.A., Mishonov, A.V., Antonov, J.I., Boyer, T.P., Garcia, H.E., Baranova, O.K., Zweng, M.M., Paver, C.R., Reagan, J.R., Johnson, D.R., 2013. World ocean atlas 2013. In: Levitus, S., Mishonov, A. (Eds.), Volume 1: Temperature, Technical Ed. NOAA Atlas NESDIS 73, p. 40.

Loukos, H., Vivier, F., Murphy, P.P., Harrison, D.E., Le Quéré, C., 2000. Interannual variability of equatorial Pacific CO2 fluxes estimated from temperature and salinity data. Geophys. Res. Lett. 27, 1735–1738.

Machado, I., Barreiro, M., Calliari, D., 2013. Variability of chlorophyll-a in the Southwestern Atlantic from satellite images: Seasonal cycle and ENSO influences. Cont. Shelf Res. 53, 102–109.

Mangum, L.J., Hayes, S.P., 1984. The vertical structure of the zonal pressure gradient in the eastern equatorial Pacific. J. Geophys. Res. Oceans 89, 10441–10449.

Martínez-López, B., Zavala-Hidalgo, J., 2009. Seasonal and interannual variability of cross-shelf transports of chlorophyll in the Gulf of Mexico. J. Mar. Syst. 77, 1–20.

Mayer, M., Alonso Balmaseda, M., Haimberger, L., 2018. Unprecedented 2015/2016 indo-Pacific heat transfer speeds up tropical Pacific heat recharge. Geophys. Res. Lett. 45, 3274–3284.

Nagura, M., McPhaden, M.J., 2008. The dynamics of zonal current variations in the central equatorial Indian Ocean. Geophys. Res. Lett. (35).

Ourmières, Y., Brasseur, P., Lévy, M., Brankart, J.M., Verron, J., 2009. On the key role of nutrient data to constrain a coupled physical–biogeochemical assimilative model of the North Atlantic Ocean. J. Mar. Syst. 75, 100–115. http://dx.doi.org/10.1016/j.jmarsys.2008.08.003, http://www.sciencedirect.com/science/article/pii/S0924796308001802.

Park, J.Y., Dunne, J.P., Stock, C.A., 2018a. Ocean chlorophyll as a precursor of ENSO: An earth system modeling study. Geophys. Res. Lett. 45, 1939–1947.

Park, J.Y., Stock, C.A., Yang, X., Dunne, J.P., Rosati, A., John, J., Zhang, S., 2018b. Modeling global ocean biogeochemistry with physical data assimilation: A pragmatic solution to the equatorial instability. J. Adv. Modelling Earth Syst. 10, 891–906. http://dx.doi.org/10.1002/2017MS001223.

Picaut, J., Hayes, S.P., McPhaden, M.J., 1989. Use of the geostrophic approximation to estimate time-varying zonal currents at the equator. J. Geophys. Res.: Oceans 94, 3228–3236.

Qiao, L., Weisberg, R.H., 1997. The zonal momentum balance of the equatorial undercurrent in the central Pacific. J. Phys. Oceanogr. 27, 1094–1119.

Radenac, M.H., Jouanno, J., Tchamabi, C.C., Awo, M., Bourlès, B., Arnault, S., Aumont, O., 2019. Physical drivers of the nitrate seasonal variability in the Atlantic cold tongue. Biogeosci. Discuss. 1–24.

Radenac, M.H., Léger, A., Delcroix, T., 2012. Sea surface chlorophyll signature in the tropical Pacific during eastern and central Pacific ENSO events. J. Geophys. Res. Oceans (117).

Raghukumar, K., Edwards, C.A., Goebel, N.L., Broquet, G., Veneziani, M., Moore, A.M., Zehr, J.P., 2015. Impact of assimilating physical oceanographic data on modeled ecosystem dynamics in the California Current System. Prog. Oceanogr. 138, 546–558.

Rio, M.H., Guinehut, S., Larnicol, G., 2011. New CNES-CLS09 global mean dynamic topography computed from the combination of GRACE data, altimetry, and in situ measurements. J. Geophys. Res. Oceans 116. http://dx.doi.org/10.1029/2010JC006505.

Rio, M.H., Mulet, S., Picot, N., 2013. New global Mean Dynamic Topography from a GOCE geoid model, altimeter measurements and oceanographic in-situ data. In: Proceedings of the ESA living planet symposium, Edinburgh.

Roemmich, D., Gilson, J., 2009. The 2004-2008 mean and annual cycle of temperature, salinity, and steric height in the global ocean from the Argo Program. Prog. Oceanogr. 82, 81–100.

Smith, N., Kessler, W.S., Cravatte, S., Sprintall, J., Wijffels, S., Cronin, M.F., Sutton, A., Serra, Y.L., Dewitte, B., Strutton, P.G., Hill, K., Sen Gupta, A., Lin, X., Takahashi, K., Chen, D., Brunner, S., 2019. Tropical Pacific observing system. Front. Mar. Sci. (6), http://dx.doi.org/10.3389/fmars.2019.00031.

Stockdale, T.N., Busalacchi, A.J., Harrison, D.E., Seager, R., 1998. Ocean modeling for ENSO. J. Geophys. Res. Oceans 103, 14325–14355.

Storto, A., Alvera-Azcárate, A., Balmaseda, M.A., Barth, A., Chevallier, M., Counillon, F., Domingues, C.M., Drevillon, M., Drillet, Y., Forget, G., 2019. Ocean reanalyses: Recent advances and unsolved challenges. Front. Mar. Sci. 6 (418).

Storto, A., Masina, S., Balmaseda, M., Guinehut, S., Xue, Y., Szekely, T., Fukumori, I., Forget, G., Chang, Y.S., Good, S.A., 2017. Steric sea level variability (1993–2010) in an ensemble of ocean reanalyses and objective analyses. Clim. Dynam. 49, 709–729.

Storto, A., Masina, S., Simoncelli, S., Iovino, D., Cipollone, A., Drevillon, M., Drillet, Y., von Schuckman, K., Parent, L., Garric, G., 2018. The added value of the multi-system spread information for ocean heat content and steric sea level investigations in the CMEMS GREP ensemble reanalysis product. Clim. Dynam. 1–26.

Szekely, T., Gourrion, J., Pouliquen, S., Reverdin, G., 2016. CORA, Coriolis Ocean Dataset for Reanalysis. SEANOE, http://dx.doi.org/10.17882/46219.

Tatebe, H., Hasumi, H., 2010. Formation mechanism of the Pacific equatorial thermocline revealed by a general circulation model with a high accuracy tracer advection scheme. Ocean Model. 35, 245–252. http://dx.doi.org/10.1016/j.ocemod.2010.07.011.

Vidard, A., Balmaseda, M., Anderson, D., 2009. Assimilation of altimeter data in the ECMWF ocean analysis system 3. Mon. Weather Rev. 137, 1393–1408.

Wang, C., Deser, C., Yu, J.Y., DiNezio, P., Clement, A., 2017. El Niño and southern oscillation (ENSO): a review. In: Coral Reefs of the Eastern Tropical Pacific. Springer, pp. 85–106.

Waters, J., Bell, M.J., Martin, M.J., Lea, D.J., 2017. Reducing ocean model imbalances in the equatorial region caused by data assimilation. Q. J. R. Meteorol. Soc. 143, 195–208.

While, J., Haines, K., Smith, G., 2010. A nutrient increment method for reducing bias in global biogeochemical models. J. Geophys. Res. Oceans (115).

Yan, C., Zhu, J., Tanajura, C.A.S., 2015. Impacts of mean dynamic topography on a regional ocean assimilation system. Ocean Sci. 11 (829).

Yu, X., McPhaden, M.J., 1999. Dynamical analysis of seasonal and interannual variability in the equatorial Pacific. J. Phys. Oceanogr. 29, 2350–2369.

Zhang, R.H., Tian, F., Zhi, H., Kang, X., 2019. Observed structural relationships between ocean chlorophyll variability and its heating effects on the ENSO. Clim. Dynam. 1–22.

Zuo, H., Balmaseda, M.A., Tietsche, S., Mogensen, K., Mayer, M., 2019. The ECMWF operational ensemble reanalysis–analysis system for ocean and sea ice: a description of the system and assessment. Ocean Sci. 15, 779–808.

Zweng, M.M., Reagan, J.R., Antonov, J.I., Locarnini, R.A., Mishonov, A.V., Boyer, T.P., Garcia, H.E., Baranova, O.K., Johnson, D.R., Seidov, D., 2013. World ocean atlas 2013. In: Levitus, S., Mishonov, A. (Eds.), Volume 2, Salinity, Technical Ed. NOAA Atlas NESDIS 74, p. 39.